Heterogeneity of foam cell biogenesis across diseases

Valentina Guerrini [1*], Brendan Prideaux [4], Rehan Khan [1], Selvakumar Subbian [1,2], Yina Wang [1], Evita Sadimin [5*], Siddhi Pawar [1], Rahul Ukey [1], Eric A. Singer [6*], Chaoyang Xue [1,3], Maria Laura Gennaro [1,2**]

[1] Public Health Research Institute, [2] Department of Medicine, and [3] Department of Microbiology, Rutgers New Jersey Medical School, Rutgers Biomedical and Health Sciences, Newark, NJ 07103
[4] Department of Neurobiology, University of Texas Medical Branch, Galveston, TX 77555
[5] Section of Urologic Pathology and [6] Section of Urologic Oncology, Rutgers Cancer Institute of New Jersey and Rutgers Robert Wood Johnson Medical School, New Brunswick, NJ 08901

***Current addresses:** Boehringer Ingelheim Animal Health, Ames, IA 50010 (VG); City of Hope National Medical Center, Duarte, CA 91010 (ES); Division of Urologic Oncology, The Ohio State University Comprehensive Cancer Center, Columbus, OH 43221 (EAS).

****Corresponding author:** marila.gennaro@rutgers.edu

Keywords: kidney disease; tuberculosis; cryptococcosis; papillary renal cell carcinoma; lipid metabolism; storage lipids

Abbreviations: CE, cholesteryl esters; H&E, hematoxylin and eosin; MALDI, matrix-assisted laser desorption/ionization mass spectrometry; MDM, monocyte-derived macrophages; pRCC, papillary renal cell carcinoma; TAG, triglycerides.

Short title: Foam cells and disease

Abstract. Foam cells are dysfunctional, lipid-laden macrophages associated with chronic inflammation of diverse origin. The long-standing paradigm that foam cells are cholesterol-laden derives from atherosclerosis research. We previously showed that, in tuberculosis, foam cells surprisingly accumulate triglycerides. Here, we utilized bacterial (*Mycobacterium tuberculosis*), fungal (*Cryptococcus neoformans*), and human papillary renal cell carcinoma (pRCC) models. We applied mass spectrometry-based imaging to assess the spatial distribution of storage lipids relative to foam-cell-rich areas in lesional tissues, and characterized lipid-laden macrophages generated under corresponding *in vitro* conditions. The *in vivo* data were consistent with in vitro findings showing that cryptococcus-infected macrophages accumulated triglycerides, while macrophages exposed to pRCC-conditioned-medium accumulated both triglycerides and cholesterol. Moreover, cryptococcus- and mycobacterium-infected macrophages accumulated triglycerides by different mechanisms. Collectively, our data indicate that the mechanisms of foam cell formation are disease-microenvironment-specific. Since foam cells are potential therapeutic targets, recognizing that their formation is disease-specific opens new biomedical research directions.

Chronic inflammation of infectious and non-infectious origin is often associated with the presence of foam cells, lipid-laden macrophages that exhibit impaired immune function and can contribute to pathogenesis [1]. Foam cells (or foamy macrophages) form when, due to dysregulated metabolism, lipids accumulate beyond the homeostatic capacity of macrophages. The lipids are stored as droplets that confer a foamy appearance to the macrophages [2]. Our understanding of foam cell biology has been largely based on studies of atherogenesis, a disease in which uptake of normal and proinflammatory lipoproteins by macrophages in the arterial wall leads to imbalanced cholesterol metabolism and formation of cholesterol-laden foam cells [3]. The accumulation of foam cells in the arterial intima leads to chronic inflammation, cell death, and tissue necrosis [3]. A similar situation is observed in tuberculosis, a chronic inflammatory disease of the lung caused by *Mycobacterium tuberculosis*. In the tuberculous lung lesions, which are called granulomas, the presence of tissue necrosis is associated with foam cell accumulation [1]. Indeed, foam cells are a hallmark of both the atherosclerotic plaque and the necrotizing tuberculous granuloma [3, 4]. We were surprised to find that the foam cells of necrotic tuberculous lung lesions are enriched in triglycerides (TAG), as demonstrated by laser-capture microdissection and mass spectrometry analysis of lesional tissue [5]. Work with cultured human macrophages and mice further established that *M. tuberculosis* infection induces TAG accumulation in macrophages [5, 6]. Thus, the atherosclerosis and tuberculosis models of foam cells are fundamentally different, indicating that foam cells may form via different mechanisms in different diseases.

To test the hypothesis that foam cell biogenesis is disease-specific, we began a study of foam cells resulting from another infectious disease, cryptococcosis, and from a form of cancer. Cryptococcosis is a clinically heterogeneous disease caused by the fungal pathogen *Cryptococcus neoformans*. It affects the lung and other organ systems, including the central nervous system, particularly in immunocompromised individuals [7]. Foamy macrophages have been observed in human tissue biopsies from pulmonary and extrapulmonary cryptococcosis [8-10] and in the lungs of infected mice [11]. Foam cells have also been associated with several forms of cancer of many organ systems that include liver, lung, colon/rectum, and kidney [12-15]. Indeed, the presence of foamy macrophages is a histological feature of papillary renal cell carcinoma (pRCC) [16, 17].

Factors released by cultured pRCC cells induce lipid accumulation in macrophages [14], indicating that the microenvironment of this tumor is lipogenic for macrophages. The nature of storage lipids and the mechanism of foam cell formation are poorly understood in these pathologies.

In the present work, we assessed the spatial distribution of foamy macrophages and storage lipids in *C. neoformans*-infected murine lungs and in human pRCC specimens. We then analyzed lipid content and the transcriptional program of lipid-laden macrophages generated under *in vitro* conditions that corresponded to these two diseases. The data established that the mechanism underlying foam cell formation varies with disease context. We can no longer base our understanding of foam cell biogenesis only on work focused on atherogenesis. Expanding our view of foam cell biogenesis may provide new targets for therapeutic intervention into diseases -- such as atherosclerosis, tuberculosis, multiple sclerosis, and certain cancers -- in which foam cell appearance and poor clinical outcome are associated (reviewed in [1]).

Results

Foamy macrophages cluster peri- or extra-lesionally and associate with TAG species in *C. neoformans*-infected murine lungs.

Foamy macrophages form during pulmonary and extrapulmonary cryptococcal infection [8, 9]. We used a model of pulmonary cryptococcosis in C57BL/6 mice to assess the spatial relationship between foam cells and neutral lipids [TAG and cholesteryl esters (CE)] in infected lungs. At 7 days post intranasal infection, infected mouse lungs exhibited several granulomatous nodular lesions visible at low magnification (**Fig. S1**). The lesions consisted of large aggregates of fungal cells surrounded by inflammatory infiltrates comprised mostly of polymorphonuclear cells, macrophages and lymphocyte aggregates, and epithelioid cells (**Fig. 1A**). Morphologically, macrophages contained small nuclei and cytoplasmic lipid droplets giving them a foamy/bubbly appearance. These foam cells tended to form clusters in peri- or extra-lesional areas of the infected foci in the lungs [hematoxylin and eosin (H&E)-stained lung slices in **Fig. 1BC**]. When we used matrix-assisted laser desorption/ionization mass spectrometry (MALDI)

imaging of sections adjacent to those used for H&E staining, we detected multiple TAG and CE species in the infected lungs (**Table S1**). All CE species localized in the fungus-rich lesions (e.g., compare H&E staining and MALDI imaging for CE 16:0 in **Fig. 1C**). In contrast, TAG species were distributed throughout the lung tissue, with some species, such as TAG 46:0, more prominently found within the lesions and others, such as TAG 50:1, found extra-lesionally (**Fig. 1C,** with corresponding ion counts in **Fig. 1D**) (see **Fig. S2** for uninfected control tissue). Localization of some TAG species and CE species in the fungus-rich lesions is consistent with the presence of TAG and sterols in fungal cells [18, 19]. In addition, the spatial distribution of some TAG species, such as TAG 50:1 in **Fig. 1C**, which was present throughout the tissue but approximately two-fold lower in the fungus-rich lesions, corresponds to that of foam cells (compare H&E staining and MALDI imaging in **Fig. 1C**), suggesting that *Cryptococcus*-induced foam cells are TAG enriched.

Fig. 1. Spatial distribution of foam cells and storage lipids in *C. neoformans*-infected murine lungs. **A-B.** H&E staining of formalin-fixed, paraffin-embedded lung sections from *C. neoformans* H99-infected mice. Images were photographed at (A) 100x magnification; scale bar is 100 μm; and (B) 400x magnification; scale bar is 10 μm. Black arrows indicate foam cells. **C.** MALDI imaging of representative CE and TAG species in infected lung sections. The left panel shows H&E staining of infected tissue sections (scale bar is 2 mm). The yellow lines delineate areas enriched in fungal cells (Crypto-rich), while the blue lines define areas enriched in foam cells (FCell-rich). The three additional panels show MALDI imaging of storage lipids in lung sections contiguous to those used for H&E staining. Representative species are shown: CE (16:0) $[M+K]^+$ *m/z* 663.48 and TAG (46:0) $[M+K]^+$ *m/z* 817.669 signals tend to correspond to cryptococci-enriched areas, while TAG (50:1) $[M+K]^+$ *m/z* 871.716 tends to be reduced in those same areas. Areas delimited by white lines correspond to some cryptococci-enriched areas in the H&E-stained section. Corresponding images of uninfected lung sections are shown in Fig. S2. **D.** Quantification of CE and TAG MALDI imaging intensity (expressed as ion count). Quantification of lipid species was performed in uninfected tissue and in fungus-rich (CN-R) and foam-cell-rich (FC-R)

areas of the infected tissue. Mean and SEM of 9 sections from three uninfected animals (3 sections per animal) and 12 sections from four infected animals (3 sections per animal) are shown. **, $p < 0.05$; ****, $p < 0.001$ (unpaired *t*-test).

Cryptococcus neoformans infection induces accumulation of TAG-rich lipid droplets in macrophages via an mTORC1-independent pathway.

MALDI imaging provides information about the spatial distribution of analytes in tissues, but it does not have the single-cell resolution needed to precisely assign a particular neutral lipid to a specific cell type. Thus, we utilized an in vitro infection model to study neutral lipid accumulation in macrophages infected with *C. neoformans*. We infected primary human monocyte-derived macrophages (MDM) with mCherry-expressing *C. neoformans* H99, quantified lipid droplet content by imaging flow cytometry, and observed a significant lipid droplet accumulation in infected macrophages (3.5-fold increase relative to uninfected cells) (**Fig. 2AB**). Lipid-droplet-enriched macrophages in the infected culture wells included both those containing fungal cells and those that did not (**Fig. 2A** and quantitative data in **Fig. S3A**). These data indicated that lipid droplet formation does not require internalization of fungal cells. Since lipid droplets accumulated in macrophages exposed to cell-free *C. neoformans* culture filtrate (**Fig. S3B**) but not in macrophages exposed to heat-killed fungi (**Fig. S3C**), lipid droplet accumulation in macrophages appears to involve a factor(s) released from live *C. neoformans* cells.

When we measured storage lipid content in *C. neoformans*-infected cells by an enzymatic assay, we found that infection increased the content of intracellular TAG but not cholesterol derivatives (**Fig. 2C**). Moreover, lipid droplet accumulation in *C. neoformans*-infected cells was essentially abrogated by treatment with an inhibitor of diglyceride acetyl transferase (DGAT), the enzyme that catalyzes the conversion of diglycerides to triglycerides (**Fig. 2D**). This finding supports the conclusion that *C. neoformans*-induced lipid droplets are TAG enriched, as previously seen with *M. tuberculosis* infection ([5] and **Fig. 2D**).

Our previous work showed that the accumulation of TAG-rich lipid droplets in macrophages infected with *M. tuberculosis* requires mTORC1 signaling, as it is inhibited

by rapamycin treatment [5]. Unlike the *M. tuberculosis* case, however, rapamycin had no effect on lipid droplet accumulation in *C. neoformans*-infected macrophages (**Fig. 2D**). Thus, even though *M. tuberculosis* and *C. neoformans* both induce accumulation of TAG-rich lipid droplets, the two pathogens do so by utilizing different signaling mechanisms.

Fig. 2. Characterization of lipid droplets induced by *C. neoformans* infection and comparisons with *M. tuberculosis*-induced effects. A. Lipid droplet content of MDM determined by imaging flow cytometry. Representative images of MDM uninfected (leftmost panel) and infected with mCherry-tagged *C. neoformans*. The two rightmost panels show macrophages in the infected culture wells carrying and not carrying intracellular fungi (orange fluorescence). Cells were stained with Bodipy 493/503 (neutral lipid dye, green fluorescence). Images were acquired by imaging flow cytometry at 24 hrs post-infection. **B.** Quantification of lipid droplet content by imaging flow cytometry expressed as median fluorescence intensity of Bodipy 493/503. Each dot represents one human donor. **C.** Neutral lipid measurements in MDM. TAG and cholesterol were measured in infected and uninfected cells using a commercially available kit. The box plots show lower quartile, median, and upper quartile of the distribution of multiple donors. The whiskers represent minimum and maximum values. The plus symbol indicates the mean. ns, non-significant; *, $p < 0.05$ (paired *t*-test). Each dot represents one human donor. **D.** Effect on lipid droplets of MDM treatment with a DGAT inhibitor (DGAT-i) or rapamycin (mTORC1 inhibitor). MDM were infected with *C. neoformans* or with *M. tuberculosis* for 24h with an MOI = 4 in both infections. DMSO (vehicle control), 0.4 nM rapamycin, or 30 nM DGAT-1 inhibitor (A922500; PubChem CID: 24768261) were added for the duration of infection. Lipid droplet content was quantified by imaging flow cytometry and expressed as Bodipy MFI, as described in panel A and in Fig. S3AB. Results are shown as ratios of Bodipy MFI of drug-treated to vehicle-treated infected cells. Mean and SD are shown. ns, non-significant; **, $p < 0.01$ (unpaired *t*-test). Each dot represents one human donor. **E-F.** Pathway analysis of the transcriptomes of *M. tuberculosis*- and *C. neoformans*-infected MDM. The two panels show Gene Ontology (GO) annotations related to metabolic processes that were (**E**)

downregulated in *M. tuberculosis*-infected MDM and (**F**) upregulated in *C. neoformans*-infected MDM, relative to uninfected control cells. The differential expression between sample classes (infected vs uninfected) was tested with coincident extreme ranks in numerical observations (CERNO). Pathways were selected using a cutoff false discovery rate of 0.05; the *p*-values for these pathways are plotted onto the x-axis. To represent effect size, pathway gene sets containing fewer genes were given greater bar height/font size than were larger sets that yielded similar *p* values. For visualization purposes, top ranking annotations are shown. Additional pathway analysis data are shown in *Supplementary Fig. S4*.

Transcriptomics identify different molecular mechanisms of TAG accumulation in *M. tuberculosis*- and *C. neoformans*-infected macrophages.

We investigated the pathways underlying TAG accumulation in *M. tuberculosis*- and *C. neoformans*- infected macrophages by conducting transcriptomics analyses of macrophages obtained from the same donors and infected in vitro with either pathogen. When we analyzed the Gene Ontology (GO) annotations related to metabolic processes, we found that the most informative signatures of macrophage metabolic reprogramming associated with TAG accumulation derived from the downregulated pathways in *M. tuberculosis*-infected macrophages and from the upregulated pathways in *C. neoformans*-infected macrophages. The former included lipid catabolism, fatty acid oxidation, oxidative phosphorylation, and electron transport chain (**Fig. 2E**), while the latter were enriched for glycolysis (**Fig. 2F**).

Metabolism-related analyses at the gene level (**Table S2** and *Supplementary text*) showed that, in *M. tuberculosis*-infected macrophages, the top three downregulated metabolic genes encoded: (i) acyl-CoA synthase (ACSM5), (ii) carnitine octanoyl transferase (CROT), which converts acyl-CoA to acyl-carnitine, a step required for transport across the mitochondrial membrane, and iii) aldehyde hydrogenase (ALDH3A2), which oxidizes fatty aldehydes to fatty acids. Downregulation of these genes likely leads to defective fatty acid oxidation. In *C. neoformans* infection, the top five upregulated metabolic genes all encoded glycolytic enzymes (**Table S3** and *Supplementary text*). We also found indicators of reduced mitochondrial functions in *C.*

neoformans-infected macrophages, including downregulation of polyribonucleotide nucleotidyl transferase 1 (PNPT1) and a glutaminyl-tRNA amidotransferase subunit 1 (QRSL1) (**Table S3**). The PNTP1 product regulates mitochondrial homeostasis and the abundance of electron transport chain components [20]. Missense mutations in the human QRSL1 locus have been associated with defects in oxidative phosphorylation [21]. In addition, several aldehyde dehydrogenases were downregulated in *C. neoformans*-infected macrophages, an indicator of reduced fatty acid oxidation (**Table S3** and *Supplementary text*).

We identified additional gene expression markers of TAG accumulation in the two infections. For example, in *M. tuberculosis* infection, we observed downregulation of lipolytic genes, upregulation of sirtuins and sirtuin-stabilizing functions, and expression changes in genes signifying increased production of ceramide and altered cellular redox. These can all lead to TAG accumulation (see **Table S2** and *Supplementary text*). In *C. neoformans* infection, additional indicators of metabolic remodeling toward TAG biosynthesis included (i) upregulation of genes for the production of dihydroxyacetone phosphate, which can be routed toward TAG biosynthesis, (ii) upregulation of hexokinase (HK2) and lactate dehydrogenase (LDHA), which indirectly inhibit lipolysis, and (iii) downregulation of AMP-activated protein kinase (AMPK), which inhibits de novo biosynthesis of fatty acids and stimulates fatty acid oxidation [22] (see **Table S3**). These and additional markers of lipid accumulation are discussed further in the *Supplementary text*.

The transcriptomics data also shed light on the requirement in *M. tuberculosis* infection for signaling by mechanistic target of rapamycin complex 1 (mTORC1) (**Fig. 2D**), which is lipogenic in multiple ways [23]. *M. tuberculosis*-infected macrophages showed downregulated TP53 gene and upregulated TP53-specific E3 ligases that target this factor for proteasomal degradation (see **Table S2** and *Supplementary text*). Decreased activity of TP53 correlates well with increased mTORC1 signaling, since TP53 induces expression of Deptor (**Table S2**) and leads to activation of AMPK, two factors that inhibit mTORC1 [24, 25].

We conclude that, with both infections, the accumulation of TAG results from decreased oxidative phosphorylation, increased glycolysis, increased lipid biosynthesis, and

decreased lipid catabolism. However, the molecular modalities of macrophage metabolic reprogramming differ between the two infections.

Foamy macrophages preferentially associate with CE- and TAG-enriched kidney areas in papillary renal cell carcinoma.

Papillary renal cell carcinoma (pRCC) is useful for studies of foam cell biogenesis in a cancer context, since foam cells are a frequent histopathologic finding in this type of cancer [16, 17]. To characterize pRCC-associated foam cells, we used pRCC specimens obtained from patients who underwent partial or radical nephrectomy and performed MALDI imaging and H&E staining of adjacent sections of the resected tissues. The foamy macrophages, which are characterized morphologically by foamy/bubbly cytoplasm and small nuclei, were seen interspersed throughout the inter-tumoral stroma. Nine CE species were detected in the pRCC tissues. Most were distributed throughout the tissue, but their localization varied with the degree of saturation of the esterified fatty acid (**Fig. S5**, **Table S1**). In particular, the two monounsaturated species (CE 16:1 and CE 18:1), which were the most abundant in the tissues, associated with highly localized, intense signals (CE 16:1 tissue localization is shown in **Fig. 3A**). In contrast, TAG species yielded only localized signals, which were similar for all detected TAGs (**Fig. 3B** shows the distribution of TAG 52:2, which is representative of all TAG species; see **Fig. S6** for other TAG species). H&E staining revealed that the intense localized CE signals corresponded to large foam cell aggregates (**Fig. 3CEG** show one such area at increasing magnification), while the TAG signals corresponded to tissue regions containing large numbers of foam cells interspersed among cancer cells (**Fig. 3DFH** show a representative area at increasing magnification). Given that CE species were detected throughout the tissue (**Fig. S6**), the TAG-rich regions also contained CE, albeit at lower levels than the large foam cell aggregates shown in the left panels of Fig. 3. In summary, MALDI imaging showed associations between foam-rich areas with TAG species, CE species, or both, suggesting that, in pRCC, foam cells may accumulate either or both classes of these storage lipids. Bioptic tissues collected from two additional patients showed similar

differential distribution of TAG and CE species in pRCC foam cells, with more intense TAG signals associated with large necrotic regions (**Fig. S7**).

Fig. 3. Spatial distribution of foam cells and storage lipids in papillary renal cell carcinoma (pRCC). A-B. MALDI imaging of representative CE and TAG species in pRCC resected tissues. MALDI-2 MSI ion distribution for CE 16:1 $[M+K]^+$ *m/z* 661.532 (panel A) and TAG 52:2 $[M+K]^+$ *m/z* 897.731 (panel B) are shown in frozen pRCC tissue sections; scale bar is 3 mm. The white rectangles delineate areas of high signal intensity that are magnified in the corresponding histology panels C-D. **C-H.** H&E staining of frozen pRCC tissue sections. Serial sections to those used for MALDI imaging were H&E stained. Each column corresponds to the top MALDI image (left panels, CE 16:1; right panels, TAG 52:2). The black box in each row marks the area of tissue shown at higher magnification in the corresponding panel below. **C-D**. scale bar is 500 mm. Black arrows in panel C mark large foam cell aggregates. The black box in C marks an area enriched for foam cell aggregates, which are further magnified in panel E. The black box in D marks an area enriched for foam cells interspersed among tumor cells, which is further magnified in panel F. **E-F.** scale bar is 150 mm. The black boxes in these panels mark areas further magnified in panels G and H, respectively. **G-H.** scale bar is 50 mm. Panel G shows a foam cell aggregate; panel H shows foam cells interspersed among tumor cells.

Factor(s) released by a papillary renal cell carcinoma-like cell line induce macrophage accumulation of both TAG and CE.

We next investigated the effects of pRCC on storage lipid accumulation in macrophages in vitro by exposing human macrophages to cell-free conditioned medium from cultures of the ACHN cell line, which is derived from a human renal cell carcinoma and exhibits pRCC features [26]. Exposure to ACHN-conditioned medium induced macrophage production of chemokines and cytokines, including IL-8, IL-6, CCL2, and CXCL16 (**Fig. S8A**), which are characteristic of the response of tumor-associated macrophages to factors released by cancer cells [27-29]. ACHN-medium-treated macrophages also exhibited lipid droplet accumulation (**Fig. 4AB**), in agreement with previous

observations [14], indicating the presence in the medium of lipogenic bioproduct(s) of the ACHN cells. Since IL-8 produced by cultured pRCC cells has been proposed as a foam-cell-inducing factor [14], we investigated the relationship among pRCC, foam cell formation, and IL-8 in our experimental system. We found that IL-8 is lipogenic for macrophages, but at a concentration ~10-fold higher than that measured in the ACHN-conditioned medium (~0.5ng/ml) (**Fig. S8BC** and **Table S4**). Thus, the lipogenic effect of the ACHN medium is unlikely due to IL-8 produced by the tumor cells. We cannot exclude, however, that IL-8 is lipogenic via paracrine-autocrine mechanisms in the tumor microenvironment in vivo since, for example, ACHN-medium-treated macrophages produce lipogenic concentrations of this cytokine (~5ng/ml) (**Fig. S8A and Table S4**).

Storage lipid analysis by enzymatic assays showed that lipid droplet accumulation in ACHN-medium-treated macrophages correlated with increased levels of both TAG and cholesterol (**Fig. 4C**). Moreover, the lipid droplet content of these macrophages decreased upon treatment with a chemical inhibitor of acyl-coenzyme A:cholesterol acyltransferase (ACAT), the enzyme that converts cholesterol to cholesteryl esters, and, to some extent, also with a DGAT inhibitor (**Fig. 4D**). These results suggest yet another context-specific mechanism of foam cell formation. Indeed, metabolism-related gene expression analysis identified mechanisms for both TAG and cholesterol accumulation. Pathways related to glycolysis featured among the top ranked Gene Ontology (GO) annotations related to metabolic processes (**Fig. 4E**). At the gene-level, the top four upregulated metabolic genes encoded glycolytic enzymes (**Table S5,** and *Supplementary text*). We also found gene markers of reduced TCA cycle, including upregulation of adenylate kinase 4 (AK4), a key metabolic regulator increasing glycolysis and inhibiting TCA cycle and oxidative phosphorylation [30], and downregulation of PPARGC1A (**Table S5**). The latter gene encodes PGC-1α, a master regulator of energy metabolism that promotes fatty acid oxidation and TCA cycle and decreases TAG storage [31] (**Table S5** and *Supplementary text*). Together, increased glycolysis and reduced TCA cycle would result in routing of pyruvate towards de novo lipogenesis.

Among additional markers of TAG accumulation is notable the increased expression of genes associated with or regulated by YAP/TAZ signaling, which regulates metastasis and metabolic reprogramming, including lipid metabolism, in cancer cells [32]. These genes include TEAD transcription factors, the perilipin PLIN5, and the fructose transporter SLC2A5 (increased fructose uptake may lead to lipogenesis via fructolysis) (**Table S5** and *Supplementary text*). Increased YAP/TAZ signaling is also supported by the above-mentioned upregulation of AK4 and downregulation of phospholipase D family member 6 (PLD6), since both gene expression changes might result in decreased activity of AMPK, which inhibits YAP/TAZ [33] (**Table S5** and *Supplementary text*). Gene expression markers of impaired fatty acid oxidation and additional mechanisms of lipid accumulation in ACHN-medium-treated macrophages are discussed in the *Supplementary text*.

The ACHN-medium-treated macrophages also exhibited gene expression changes associated with dysregulation of cholesterol metabolism. For example, the scavenger receptor CD36, which is a key regulator of cholesterol homeostasis, was downregulated, presumably as a consequence of PPARGC1A downregulation [31] (**Table S5**). CD36 induces cholesterol depletion by promoting macrophage cholesterol efflux and proteasomal degradation of HMG-CoA reductase, the rate-limiting enzyme in sterol synthesis [34]. An additional marker of dysregulated cholesterol homeostasis is the downregulation of adenylate cyclase (ADCY1), which generates cAMP signaling for cholesterol efflux in atherogenic foam cells [35]. The above-proposed increased YAP/TAZ signaling might also result in cholesterol accumulation, since YAP/TAZ is involved in the metabolism of fatty acids and sterols [32].

Collectively, gene expression data point toward macrophage metabolic reprogramming in response to factors in the ACHN-conditioned medium. This reprogramming includes increased glycolysis, impaired TCA cycle and oxidative metabolism, decreased lipolysis, and dysregulated cholesterol homeostasis.

Fig. 4. Characterization of the lipogenic effects of treatment of human primary macrophages with conditioned medium from ACHN cell cultures. Monocyte-derived macrophages (MDM) were incubated with ACHN-conditioned medium; lipid

droplet and neutral lipid content was measured after 7 days of treatment. **A.** Lipid droplet content of MDM determined by imaging flow cytometry. Representative images of MDM untreated and ACHN-treated stained with Bodipy 493/503 (neutral lipid dye, green fluorescence) acquired by imaging flow cytometry. **B.** Quantification of lipid droplet content by imaging flow cytometry expressed as median fluorescence intensity (MFI) of Bodipy 493/503. Each dot represents one human donor. **C.** Neutral lipid measurements in MDM. TAG and cholesterol were measured in infected and uninfected cells using a commercially available kit. The box plots show lower quartile, median, and upper quartile of the distribution of multiple donors. The whiskers represent minimum and maximum values. The plus symbol indicates the mean. *, $p < 0.05$; **, $p < 0.01$ (Wilcoxon signed-rank test). D. Effect on lipid droplets of MDM treatment with a DGAT inhibitor and an ACAT inhibitor. MDM were treated with ACHN-conditioned medium containing DMSO (vehicle control), 90 nm DGAT-1 inhibitor (DGAT-i) (A922500; PubChem CID:24768261), or 10 μM ACAT inhibitor (ACAT-i) (PubChem CID:10019206) for 7 days. Lipid droplet content was quantified by imaging flow cytometry and expressed as Bodipy MFI,as described in Fig. 2A. Results are shown as ratios of Bodipy MFI of drug-treated to vehicle-treated cells. Mean and SD are shown. ns, non-significant; **, $p < 0.01$ (unpaired *t*-test). Each dot represents one human donor. E**.** Pathway analysis of the transcriptome of ACHN-medium-treated MDM. The panel shows Gene Ontology (GO) annotations related to metabolic processes that were upregulated in ACHN-medium-treated MDM, relative to untreated control cells. The differential expression between sample classes (infected vs uninfected) was tested with coincident extreme ranks in numerical observations (CERNO). Pathways were selected using a cutoff false discovery rate of 0.055; the *p*-values for these pathways are plotted onto the x-axis. To represent effect size, pathway gene sets containing fewer genes were given greater bar height/font size than were larger sets that yielded similar *p* values. It is noted that immunoglobulin production by macrophages in the context of tumor microenvironments has been described [42] - it is not discussed as it does not appear relevant to the topic of our report. Additional pathway analysis data are shown in *Supplementary Fig. S9*.

Discussion

The data reported above show that the mechanisms of foam cell biogenesis differ with disease context. That is the case regardless of the chemical nature of the storage lipids they accumulate. For example, macrophages infected with *M. tuberculosis* and *C. neoformans* are enriched in TAG, as demonstrated by the drastic lipid droplet decrease caused by pharmacological inhibition of TAG biosynthesis in the two infections. In both cases, the accumulation of TAG likely results from a switch from oxidative to glycolytic metabolism that includes increased biosynthesis and decreased catabolism of lipids. However, the molecular mechanisms underlying the metabolic reprogramming of macrophages differ between the two infections, as indicated by the different effect of rapamycin on lipid droplet accumulation in the two infections. Still other mechanisms are likely at play in pRCC-associated macrophages, which accumulate neutral lipids by reprogramming both cholesterol and TAG metabolism. Moreover, although gene expression levels do not directly translate into protein levels, protein activity, and metabolic fluxes, the gene expression data presented above clearly imply that the metabolic remodeling leading to neutral lipid accumulation occurs through signaling, regulatory, and effector mechanisms that are specific to each experimental condition. Therefore, our data show that macrophage foam cells in different diseases are mechanistically heterogeneous even though they may be similar histochemically (lipid droplets consistently confer a “pale bubbly” appearance upon H&E staining) and perhaps even functionally, as discussed below.

A key to understanding foam cell heterogeneity is the biochemical diversity of the microenvironments driving their biogenesis. It is well established that uptake of exogenous lipids can drive foam cell formation. This is the case in atherogenesis, where sequestration of cholesterol-rich lipoproteins in the arterial wall leads to endothelial activation, recruitment of monocytes, and monocyte differentiation into lipoprotein-ingesting phagocytes that become foam cells [3]. Moreover, in some cancers, such as colon cancer, the fatty acid-enriched environment induces lipid droplet accumulation in tumor-associated macrophages [15]. It would be fallacious, however, to associate foam cell formation exclusively with exogenous lipid uptake. Instead, our work points to

additional scenarios in which various microenvironment-specific signals trigger a metabolic remodeling of local macrophages that leads to excess intracellular fatty acids that are detoxified by storage in droplets. These environmental triggers may include pathogen-derived molecules, cancer cell products, inflammatory signals from activated and/or damaged cells that, for example, activate Toll-like receptors (TLR) (or other pattern recognition receptors) resulting in the reshaping of the macrophage lipidome [36]. Additional heterogeneity may result from the combinatorial effects of multiple foam-cell-inducing signals in some microenvironments. For example, foam cells may be induced in pRCC by yet unidentified cancer cell products, as indicated by our results with ACHN-conditioned medium, together with lipogenic proinflammatory cytokines, such as IL-8, produced by tumor-associated-macrophages. Moreover, additional mediators might be produced by cell types that are not represented in our in vitro system, such as the lipid-filled tumor cells that we observed in the pRCC bioptic tissue. In tuberculosis, we showed that, in addition to bacterial components that presumably trigger TLR2 signaling [37, 38], macrophage lipid accumulation requires another lipogenic proinflammatory cytokine, TNFα, produced by infected macrophages [5]. In cryptococcosis, the lung epithelial cells secrete IL-8 [11], suggesting a possible role of this cytokine in cryptococcal foam cell formation. Additional work is needed to identify the exogenous (i.e., generated by microbes, cancer cells, or other cell types) trigger signals and to determine how commonly foam cells are induced by combinations of exogenous and autocrine/paracrine signals.

It is reasonable to assume that, despite the different mechanisms of biogenesis, the presence of foam cells represents a maladaptive immune response in all the pathological contexts they form. Generally, lipid-laden macrophages tend to lose protective immune functions, including phagocytosis, efferocytosis, and autophagy. They can also induce tissue damage, contribute to necrosis, exhibit impaired antimicrobial activity, and even sustain survival of intracellular pathogens (reviewed in [1]). Indeed, given their contribution to pathogenesis, foam cells have been recognized as targets of pharmacological intervention, for example in atherosclerosis and some cancers [15, 39]. Moreover, foam cells are often associated with kidney disease, such as focal and segmental glomerulosclerosis and diabetic nephropathy [40], in addition to

the pRCC investigated in the present work. Their pathophysiological significance in the kidney remains puzzling, and all mechanistic hypotheses on their biogenesis derive from the atherosclerosis literature [40]. Recognizing that foam cells do not result only from macrophage uptake of exogenous lipids and that the mechanisms of their formation are microenvironment-specific opens new directions for mechanistic and drug development research of high biomedical significance.

Materials and Methods

Cell cultures. Peripheral blood mononuclear cells (PBMC) were isolated and monocyte-derived macrophages (MDM) were generated as previously described [5]. Briefly, human blood was obtained from the New York Blood Center (Long Island City, NY, USA), and PBMC were isolated by Ficoll density gradient centrifugation (Ficoll-Paque, GE Healthcare, Uppsala, Sweden). Isolated PBMC were washed and resuspended in serum-free RPMI-1640 medium (Corning, Manassas, VA, USA) supplemented with 4 mM L-glutamine (Corning, Manassas, VA, USA) and seeded at a density of 1×10^7 cells/ml in tissue culture multiwell plates or flasks. After 4 hr, non-adherent cells were removed by washing five times with 1× PBS (Corning, Manassas, VA, USA) and the adherent fraction was cultured over 7 days in complete RPMI medium (RPMI-1640 supplemented with 10% fetal bovine serum (Seradigm, Radnor, PA, USA) and 4 mM L-glutamine.
The ACHN cell line was obtained from the American Type Culture Collection (ATCC). To obtain conditioned medium, cells were grown in complete RPMI for 6-9 passages in humidified atmospheric air containing 5% CO_2 at 37°C. Cell culture medium was collected 24 hr after the last passage, filtered through a 0.4 μM filter to remove any cell debris, and stored in aliquots at -80°C.

Pathogens. mCherry-expressing *M. tuberculosis* $H_{37}Rv$ strain was grown in liquid medium to mid-log phase and frozen stocks prepared for macrophage infection as described (5). mCherry-expressing *C. neoformans* H99 strain was grown in YPD medium overnight at 30°C with constant agitation, washed three times with 1× PBS, and

resuspended in 1× PBS before use in macrophage infection. The final fungal concentration was adjusted to 1 x 10^8 cell/ml with complete RPMI medium [RPMI-1640 supplemented with 10% heat-inactivated fetal bovine serum (Seradigm, Radnor, PA, USA) and 4 mM L-glutamine]. A suspension of heat-killed *C. neoformans* was prepared by resuspending the fungal cells in 1× PBS and incubating the suspension at 75°C for 1 hr in a heat block. To prepare cell-free culture supernatant, *C. neoformans* H99 was grown in complete RPMI medium for 24 hr (end of logarithmic growth phase), filtered through a 0.2 μM filter, and used for macrophage treatments.

Macrophage treatments. For infection experiments, following 7 days of MDM differentiation, MDM were counted and infected with either *M. tuberculosis or C. neoformans*. The pathogen inoculum for infection was prepared by adding the microorganisms to supplemented RPMI-1640 medium (as above) to obtain an MOI of 4 colony-forming units (cfu) per cell. Pathogen clumps were disrupted by vortexing with sterile 3-mm-diameter glass beads for 2 min; this suspension was used for MDM infection. MDM were incubated with *M. tuberculosis* for 24h. MDM were infected with *C. neoformans* for 3 h, washed with 1× PBS three times, and incubated with fresh medium for 24 hr. When chemical inhibitors were tested, they were added to the MDM at the time of infection. For treatment of uninfected MDMs with recombinant TNFα, the cytokine was incubated with the MDMs for 24 hr.
At 24 hr post-infection, supernatants were collected and frozen for cytokine analysis and MDM were washed with 1× PBS three times and collected for subsequent analysis.
For treatment with ACHN conditioned medium or IL-8 recombinant cytokine (Abcam, Cambridge, England), after PBMC isolation, the adherent fraction of PBMC was treated with conditioned medium (50% fresh medium and 50% conditioned medium) or IL-8 for 7 days. Medium was replaced at 3 and 6 days of incubation. At day 7 post-treatment, supernatants were collected and frozen for cytokine analysis, and MDM were washed with 1× PBS three times and collected for subsequent analysis.
Cytokine or chemical inhibitor doses were selected based on available EC_{50} data and toxicity profiles with untreated macrophages (Trypan Blue staining or MTS assay; CellTiter 96 Aqueous One Solution Cell Proliferation Assay Promega, Madison, WI,

USA). Only inhibitor doses resulting in >90% cell viability were utilized. The following concentrations were used: 30-90 nM DGAT inhibitor A922500 (PubChem CID: 24768261) (Santa Cruz Biotechnology, Dallas, TX, USA), 0.4 nM rapamycin (mTORC1 inhibitor) (Selleckchem, Houston, TX, USA), 10 μM ACAT inhibitor (PubChem CID: 10019206) (Santa Cruz Biotechnology, Dallas, TX, USA), and 0.2-6 ng/ml recombinant IL-8 (Research and Diagnostic Systems, Minneapolis, MN, USA).

Imaging flow cytometry. Imaging flow cytometry of MDM was performed as previously described [5]. MDM were detached from tissue culture plates by incubating with 5 mM EDTA in 1× PBS pH 8 for 30 min followed by gentle scraping, washed once with 1× PBS, and fixed with 4% paraformaldehyde in 1× PBS for 45 min at room temperature. Cells were then washed with 1× PBS containing 0.1% bovine serum albumin (PBS-BSA), resuspended in 50 μl of PBS-BSA containing 5 μl of Fc receptor blocking solution, FcX (BioLegend, San Diego, CA), and incubated at room temperature for 5 min. After incubation, 50 μl of PBS-BSA containing 2.5 μl of CD11c APC antibody (clone S-HCL-3) or 5 μl of CD11c BV421 antibody (clone B-ly6 RUO) (BD Biosciences) were added to each tube, and samples were incubated at 4°C for 30 min. After washing with PBS-BSA, cells were stained with 0.3 μg/ml Bodipy 493/503 (Life Technologies, Carlsbad, CA) in 1× PBS for 15 min. For each experimental condition, data from 5,000–10,000 CD11c+ cells were acquired with an ImageStream^{X}Mark II imaging flow cytometer (Amnis Corporation, Seattle, WA) using 60× magnification. Image data were analyzed by IDEAS software version 6.0 (Amnis Corporation, Seattle, WA) after applying a compensation matrix and selecting the region of interest (lipid droplets) with the Spot Mask tool. Median fluorescence intensity and spots per cell were extracted.

Lipid quantification in macrophages. MDM were detached from the cell culture plates as described above and transferred to microcentrifuge tubes. Cell pellets were obtained by culture centrifugation at 300*x g* and frozen for subsequent lipid measurement. Triglyceride-Glo™ Assay and Cholesterol/Cholesterol Ester-Glo™ Assay kits (Promega; Madison, WI, USA) were used to quantify triglycerides and cholesterol, following the manufacturer's instructions. Cholesterol was quantified following addition of cholesteryl

esterase to convert cholesteryl esters to free cholesterol, following manufacturer's instructions.

Mouse infection and tissue collection. Female mice with an average weight of 20-25 g were used. C57BL/6 mice were purchased from the Jackson Laboratories. Animal studies were performed at the Public Health Research Institute Animal facility. All studies were conducted following biosafety level 2 (BSL-2) protocols and procedures approved by the Institutional Animal Care and Use Committee (IACUC) and Institutional Biosafety Committee of Rutgers University under protocol 999901066. *C. neoformans* wild type strain H99 was cultured on YPD medium. To prepare fungal cells for infection, an overnight culture of *C. neoformans* H99 was washed three times with 1× PBS and the concentration of yeast cells was determined by hemocytometer counting. The final fungal concentration was adjusted with PBS to 2 x 10^6 cell/ml. Each mouse was infected intranasally with 1 x 10^5 H99 cells in a 50 µl volume after being anesthetized with a mix of Ketamine (12.5 mg/mL) and Xylazine (1 mg/mL). After infection, animals were weighed daily and monitored twice daily for progression of disease, including weight loss, gait changes, labored breathing, and fur ruffling. Infected animals were sacrificed at day 7 post-infection, according to the experimental design and the Rutgers University IACUC approved animal protocol. A part of the dissected lung tissues was fixed in 10% formalin solution and sent to the Rutgers histopathological core facility for section preparation and staining with hematoxylin and eosin (H&E) using standard protocols. Another portion of the lung tissues was placed on labeled plastic cryohistology trays and frozen on dry ice for 2 minutes in a Styrofoam container. The samples were then wrapped with aluminum foil and stored in labeled Ziploc bags at -80°C until use for MALDI imaging.

Human Biopsies. Papillary renal cell carcinoma tissue was obtained from the Rutgers CINJ Biorepository. Tissue collected during surgery was frozen by the Biorepository using the PrestoCHILL machine, which allows for ultrafast freezing. All tissues analyzed derived from radical nephrectomies; the RWJUH surgical pathology reports indicated papillary renal cell carcinoma, type 1, WHO grade 2. Utilization of archived de-identified

biospecimens from the Rutgers Cancer Institute of New Jersey Biospecimen Repository Services (BRS) Shared Resources was performed under IRB protocols 001006 and 002002.

Matrix-assisted laser desorption/ionization (MALDI) mass spectrometry. Frozen lung samples were used to prepare 12 µm-thick cryosections using a Leica CM1860 cryostat. Tissue sections were mounted onto indium tin oxide coated glass slides (Delta Technologies Limited, Loveland, Colorado) and stored individually in Ziploc bags at -80°C. Adjacent sections were prepared on Superfrost Plus™ glass microscope slides (Fisherbrand) for H&E staining, which was performed using standard protocols at the UTMB Histology core. Sections for MALDI imaging were coated with 2′,4′,6′-Trihydroxyacetophenone monohydrate at 10 mg/ml in 50:50 cyclohexane/methanol using a HTX TM Sprayer. 20 passes were performed over each tissue at a spray volume of 50 ml/min and nozzle temperature of 50°C. Once sprayed, samples were placed individually in Ziploc bags and immediately transferred to a -80°C freezer for storage. Following MALDI-MS image acquisition, matrix was removed from the slides by serial rinses in 50% ethanol, and tissue sections were allowed to airdry at room temperature for 30 min. The tissue sections were then transferred to the UTMB histology core for H&E and Oil Red staining using standard protocols.
MALDI MS imaging was performed using a Q-Exactive HF mass spectrometer (Thermo Scientific, Bremen, DE) fitted with a MALDI/ESI Injector (Spectroglyph LLC, Kennewick, WA). Laser post-ionization (MALDI-2) was used to enhance analytical sensitivity for triglycerides and cholesteryl esters. Images were acquired at 20 micrometer voxel size, using a pulse energy of ~6 mJ and repetition rate of 30Hz. Q Exactive HF MS Scan parameters were optimized for triglyceride and cholesteryl ester detection: polarity – positive, scan range – 350-1500 m/z, resolution – 120,000, automatic gain control - off, maximum inject time 250 ms. ImageInsight™ (Spectroglyph LLC) software was used for initial data visualization and to convert data files into imzML format for visualization and further processing in SCiLS™ software (Bruker, Billerica, MA). TAG and CE species were predominantly detected as potassium adducts and lipid identifications were

assigned within a 3pm mass tolerance range using Lipid Maps database. All lipid images produced were normalized to the total ion chromatogram.

Cytokine measurement. A panel of cytokines/chemokines/growth factors was measured using Luminex technology at the Rutgers Immune Monitoring and Advanced Genomics Core Facility. Assays were performed in microtiter plates and plates were read with the Luminex 200 instrument. Each sample was measured in duplicate.

Transcriptomics and pathway analysis. RNA was isolated by using TRI reagent (Molecular Research Center, Cincinnati, OH, USA) according to manufacturer's instructions. RNA-Seq was conducted at the Rutgers Genomics Center. The quality of RNA was first assessed for integrity on an Agilent TapeStation using high sensitivity RNA kit, PN-5067-5579 (Agilent technologies Inc, CA). Samples with RNA integrity number (RIN) >7.0 were considered to have sufficient quality for subsequent processing. Illumina compatible cDNA libraries generated for polyA selected mRNA using NEB next ultra RNA library preparation kit Cat#E7530L (New England Biolabs Inc, MA). The cDNA libraries were purified using AmpureXP beads, Product No: A63882 (Beckman Coulter) and analyzed on an Agilent TapeStation using HS D1000 screen tape PN- 5067-5584 (Agilent Technologies Inc, CA) to estimate the size of the library and quantitated using Qubit 4 Fluorometer, using HS reagent kit, Cat. No. Q33231 (Thermofisher Scientific, MA). Equimolar amounts of barcoded libraries pooled together and sequenced on Illumina NovaSeq 6000 Instrument (Illumina, San Diego, CA) using SP flow cells kits (cat # 20040326) with 2x150 cycles configuration.
Read count and gene-level transcript abundance analysis were performed by the Rutgers Molecular and Genomics Informatics Core. In brief, raw transcriptome reads were assessed for quality control (FASTQC v0.11.8) and trimmed for quality and adapter contaminant (cutadapt v 2.5). Trimmed reads were aligned to the mouse genome (GRCh37) using STAR (v2.6.1), followed by transcript abundance calculation and hit count extraction with StringTie (v2.0) and featureCounts (v1.6.4), respectively. The differential expression between sample classes (treated vs non treated for each condition) was tested with coincident extreme ranks in numerical observations

(CERNO) [41] for metabolism-related Gene Ontology gene sets. The Benjamini–Hochberg method was used to calculate the false discovery rate (FDR). Gene sets (pathways) were identified at a cutoff false discovery rate of 0.05. Genes in differentially expressed metabolism-related Gene Ontology gene sets having FDR < 0.05 were selected based on individual p value ($p << 0.05$) and ranked by log2 fold change (treated vs non-treated in each condition) and number of occurrences in the differentially expressed gene sets. The top five down- and up-regulated genes were selected for further analysis. Differentially expressed genes ($p < 0.05$) reported in the published literature as functionally related to the top five up- and down-regulated genes in each condition were also selected for analysis and data interpretation.

Acknowledgements. We thank Knowledge Synthesis, Inc. for help with statistical analyses of the transcriptomics data; Karl Drlica for critical reading of the manuscript. This work was funded by NIH grants R01 HL149450, R01 HL149450-S1, R01 AI158911 (M.L.G.), R01AI155647, R01AI169769 (C.X.), P30CA072720 (E.S and E.A.S), and a Cancer Prevention and Research Institute of Texas (CPRIT) High Impact High Risk grant RP190669 (B.P). MLG also acknowledges funding through NJ ACTS (NIH UL1TR003017).

References

1. Guerrini V, Gennaro ML. Foam Cells: One Size Doesn't Fit All. Trends Immunol. 2019;40(12):1163-79. Epub 2019/11/17. doi: 10.1016/j.it.2019.10.002. PubMed PMID: 31732284; PubMed Central PMCID: PMCPMC6925453.
2. den Brok MH, Raaijmakers TK, Collado-Camps E, Adema GJ. Lipid Droplets as Immune Modulators in Myeloid Cells. Trends Immunol. 2018;39(5):380-92. Epub 2018/02/27. doi: 10.1016/j.it.2018.01.012. PubMed PMID: 29478771.
3. Moore KJ, Sheedy FJ, Fisher EA. Macrophages in atherosclerosis: a dynamic balance. Nat Rev Immunol. 2013;13(10):709-21. doi: 10.1038/nri3520. PubMed PMID: 23995626; PubMed Central PMCID: PMCPMC4357520.
4. Russell DG, Cardona PJ, Kim MJ, Allain S, Altare F. Foamy macrophages and the progression of the human tuberculosis granuloma. Nat Immunol. 2009;10(9):943-8. PubMed PMID: 19692995.
5. Guerrini V, Prideaux B, Blanc L, Bruiners N, Arrigucci R, Singh S, et al. Storage lipid studies in tuberculosis reveal that foam cell biogenesis is disease-specific. PLoS Pathog. 2018;14(8):e1007223. Epub 2018/08/31. doi: 10.1371/journal.ppat.1007223. PubMed PMID: 30161232; PubMed Central PMCID: PMCPMC6117085 following competing interests: Hugh Salamon is affiliated to the commercial company Knowledge Synthesis Inc.
6. Dawa S, Menon D, Arumugam P, Bhaskar AK, Mondal M, Rao V, et al. Inhibition of Granuloma Triglyceride Synthesis Imparts Control of Mycobacterium tuberculosis Through Curtailed Inflammatory Responses. Front Immunol. 2021;12:722735. Epub 20210915. doi: 10.3389/fimmu.2021.722735. PubMed PMID: 34603294; PubMed Central PMCID: PMCPMC8479166.
7. Maziarz EK, Perfect JR. Cryptococcosis. Infect Dis Clin North Am. 2016;30(1):179-206. doi: 10.1016/j.idc.2015.10.006. PubMed PMID: 26897067; PubMed Central PMCID: PMCPMC5808417.
8. Karmakar P, Jeyarajah R, Ramasubramanian V. Isolated cryptococcal osteomyelitis in immunocompetent patient. J Indian Med Assoc. 2011;109(8):592, 4. PubMed PMID: 22315871.

9. Thornton CS, Larios O, Grossman J, Griener TP, Vaughan S. Pulmonary Cryptococcus infections as a manifestation of idiopathic CD4 lymphocytopenia: case report and literature review. BMC Infect Dis. 2019;19(1):862. Epub 20191017. doi: 10.1186/s12879-019-4453-x. PubMed PMID: 31623573; PubMed Central PMCID: PMCPMC6798450.
10. Howard-Jones AR, Sparks R, Pham D, Halliday C, Beardsley J, Chen SC. Pulmonary Cryptococcosis. J Fungi (Basel). 2022;8(11). Epub 20221031. doi: 10.3390/jof8111156. PubMed PMID: 36354923; PubMed Central PMCID: PMCPMC9696922.
11. Normile TG, Bryan AM, Del Poeta M. Animal Models of Cryptococcus neoformans in Identifying Immune Parameters Associated With Primary Infection and Reactivation of Latent Infection. Front Immunol. 2020;11:581750. Epub 20200915. doi: 10.3389/fimmu.2020.581750. PubMed PMID: 33042164; PubMed Central PMCID: PMCPMC7522366.
12. Donadon M, Torzilli G, Cortese N, Soldani C, Di Tommaso L, Franceschini B, et al. Macrophage morphology correlates with single-cell diversity and prognosis in colorectal liver metastasis. J Exp Med. 2020;217(11). doi: 10.1084/jem.20191847. PubMed PMID: 32785653; PubMed Central PMCID: PMCPMC7596819.
13. Liu-Jarin X, Stoopler MB, Raftopoulos H, Ginsburg M, Gorenstein L, Borczuk AC. Histologic assessment of non-small cell lung carcinoma after neoadjuvant therapy. Mod Pathol. 2003;16(11):1102-8. Epub 2003/11/14. doi: 10.1097/01.MP.0000096041.13859.AB. PubMed PMID: 14614049.
14. Krawczyk KM, Nilsson H, Allaoui R, Lindgren D, Arvidsson M, Leandersson K, et al. Papillary renal cell carcinoma-derived chemerin, IL-8, and CXCL16 promote monocyte recruitment and differentiation into foam-cell macrophages. Lab Invest. 2017;97(11):1296-305. Epub 2017/08/02. doi: 10.1038/labinvest.2017.78. PubMed PMID: 28759013; PubMed Central PMCID: PMCPMC5668481.
15. Wu H, Han Y, Rodriguez Sillke Y, Deng H, Siddiqui S, Treese C, et al. Lipid droplet-dependent fatty acid metabolism controls the immune suppressive phenotype of tumor-associated macrophages. EMBO Mol Med. 2019;11(11):e10698. Epub

20191010. doi: 10.15252/emmm.201910698. PubMed PMID: 31602788; PubMed Central PMCID: PMCPMC6835560.
16. Onishi T, Ohishi Y, Goto H, Suzuki M, Miyazawa Y. Papillary renal cell carcinoma: clinicopathological characteristics and evaluation of prognosis in 42 patients. BJU Int. 1999;83(9):937-43. doi: 10.1046/j.1464-410x.1999.00094.x. PubMed PMID: 10368232.
17. Delahunt B, Eble JN. Papillary renal cell carcinoma: a clinicopathologic and immunohistochemical study of 105 tumors. Mod Pathol. 1997;10(6):537-44. PubMed PMID: 9195569.
18. Chrissian C, Camacho E, Kelly JE, Wang H, Casadevall A, Stark RE. Solid-state NMR spectroscopy identifies three classes of lipids in Cryptococcus neoformans melanized cell walls and whole fungal cells. J Biol Chem. 2020;295(44):15083-96. Epub 20200828. doi: 10.1074/jbc.RA120.015201. PubMed PMID: 32859751; PubMed Central PMCID: PMCPMC7606693.
19. Singh A, MacKenzie A, Girnun G, Del Poeta M. Analysis of sphingolipids, sterols, and phospholipids in human pathogenic Cryptococcus strains. J Lipid Res. 2017;58(10):2017-36. Epub 20170815. doi: 10.1194/jlr.M078600. PubMed PMID: 28811322; PubMed Central PMCID: PMCPMC5625125.
20. Wang G, Chen HW, Oktay Y, Zhang J, Allen EL, Smith GM, et al. PNPASE regulates RNA import into mitochondria. Cell. 2010;142(3):456-67. doi: 10.1016/j.cell.2010.06.035. PubMed PMID: 20691904; PubMed Central PMCID: PMCPMC2921675.
21. Kohda M, Tokuzawa Y, Kishita Y, Nyuzuki H, Moriyama Y, Mizuno Y, et al. A Comprehensive Genomic Analysis Reveals the Genetic Landscape of Mitochondrial Respiratory Chain Complex Deficiencies. PLoS Genet. 2016;12(1):e1005679. Epub 20160107. doi: 10.1371/journal.pgen.1005679. PubMed PMID: 26741492; PubMed Central PMCID: PMCPMC4704781.
22. Foretz M, Even PC, Viollet B. AMPK Activation Reduces Hepatic Lipid Content by Increasing Fat Oxidation In Vivo. Int J Mol Sci. 2018;19(9). Epub 20180919. doi: 10.3390/ijms19092826. PubMed PMID: 30235785; PubMed Central PMCID: PMCPMC6164956.

23. Soliman GA. The integral role of mTOR in lipid metabolism. Cell Cycle. 2011;10(6):861-2. Epub 20110315. doi: 10.4161/cc.10.6.14930. PubMed PMID: 21325894; PubMed Central PMCID: PMCPMC3100868.
24. Chen H, Shen F, Sherban A, Nocon A, Li Y, Wang H, et al. DEP domain-containing mTOR-interacting protein suppresses lipogenesis and ameliorates hepatic steatosis and acute-on-chronic liver injury in alcoholic liver disease. Hepatology. 2018;68(2):496-514. Epub 20180521. doi: 10.1002/hep.29849. PubMed PMID: 29457836; PubMed Central PMCID: PMCPMC6097912.
25. Feng Z, Zhang H, Levine AJ, Jin S. The coordinate regulation of the p53 and mTOR pathways in cells. Proc Natl Acad Sci U S A. 2005;102(23):8204-9. Epub 20050531. doi: 10.1073/pnas.0502857102. PubMed PMID: 15928081; PubMed Central PMCID: PMCPMC1142118.
26. Sinha R, Winer AG, Chevinsky M, Jakubowski C, Chen YB, Dong Y, et al. Analysis of renal cancer cell lines from two major resources enables genomics-guided cell line selection. Nat Commun. 2017;8:15165. Epub 20170510. doi: 10.1038/ncomms15165. PubMed PMID: 28489074; PubMed Central PMCID: PMCPMC5436135.
27. Cho SW, Kim YA, Sun HJ, Kim YA, Oh BC, Yi KH, et al. CXCL16 signaling mediated macrophage effects on tumor invasion of papillary thyroid carcinoma. Endocr Relat Cancer. 2016;23(2):113-24. Epub 20151111. doi: 10.1530/erc-15-0196. PubMed PMID: 26559672.
28. Xu H, Lai W, Zhang Y, Liu L, Luo X, Zeng Y, et al. Tumor-associated macrophage-derived IL-6 and IL-8 enhance invasive activity of LoVo cells induced by PRL-3 in a KCNN4 channel-dependent manner. BMC Cancer. 2014;14:330. Epub 20140510. doi: 10.1186/1471-2407-14-330. PubMed PMID: 24885636; PubMed Central PMCID: PMCPMC4024187.
29. Li D, Ji H, Niu X, Yin L, Wang Y, Gu Y, et al. Tumor-associated macrophages secrete CC-chemokine ligand 2 and induce tamoxifen resistance by activating PI3K/Akt/mTOR in breast cancer. Cancer Sci. 2020;111(1):47-58. Epub 20191219. doi: 10.1111/cas.14230. PubMed PMID: 31710162; PubMed Central PMCID: PMCPMC6942430.

30. Fujisawa K, Terai S, Takami T, Yamamoto N, Yamasaki T, Matsumoto T, et al. Modulation of anti-cancer drug sensitivity through the regulation of mitochondrial activity by adenylate kinase 4. Journal of Experimental & Clinical Cancer Research. 2016;35(1):48. doi: 10.1186/s13046-016-0322-2.
31. Cheng CF, Ku HC, Lin H. PGC-1α as a Pivotal Factor in Lipid and Metabolic Regulation. Int J Mol Sci. 2018;19(11). Epub 20181102. doi: 10.3390/ijms19113447. PubMed PMID: 30400212; PubMed Central PMCID: PMCPMC6274980.
32. Yamaguchi H, Taouk GM. A Potential Role of YAP/TAZ in the Interplay Between Metastasis and Metabolic Alterations. Front Oncol. 2020;10:928. Epub 2020/07/01. doi: 10.3389/fonc.2020.00928. PubMed PMID: 32596154; PubMed Central PMCID: PMCPMC7300268.
33. Mo JS, Meng Z, Kim YC, Park HW, Hansen CG, Kim S, et al. Cellular energy stress induces AMPK-mediated regulation of YAP and the Hippo pathway. Nat Cell Biol. 2015;17(4):500-10. Epub 20150309. doi: 10.1038/ncb3111. PubMed PMID: 25751140; PubMed Central PMCID: PMCPMC4380774.
34. Rodrigue-Way A, Caron V, Bilodeau S, Keil S, Hassan M, Lévy E, et al. Scavenger receptor CD36 mediates inhibition of cholesterol synthesis via activation of the PPARγ/PGC-1α pathway and Insig1/2 expression in hepatocytes. Faseb j. 2014;28(4):1910-23. Epub 20131226. doi: 10.1096/fj.13-240168. PubMed PMID: 24371122.
35. Tang W, Ma W, Ding H, Lin M, Xiang L, Lin G, et al. Adenylyl cyclase 1 as a major isoform to generate cAMP signaling for apoA-1-mediated cholesterol efflux pathway. J Lipid Res. 2018;59(4):635-45. Epub 20180214. doi: 10.1194/jlr.M082297. PubMed PMID: 29444935; PubMed Central PMCID: PMCPMC5880494.
36. Hsieh WY, Zhou QD, York AG, Williams KJ, Scumpia PO, Kronenberger EB, et al. Toll-Like Receptors Induce Signal-Specific Reprogramming of the Macrophage Lipidome. Cell Metab. 2020;32(1):128-43.e5. Epub 20200608. doi: 10.1016/j.cmet.2020.05.003. PubMed PMID: 32516576; PubMed Central PMCID: PMCPMC7891175.
37. Bedard M, van der Niet S, Bernard EM, Babunovic G, Cheng TY, Aylan B, et al. A terpene nucleoside from M. tuberculosis induces lysosomal lipid storage in foamy

macrophages. J Clin Invest. 2023;133(6). Epub 20230315. doi: 10.1172/jci161944. PubMed PMID: 36757797; PubMed Central PMCID: PMCPMC10014106.
38. Almeida PE, Silva AR, Maya-Monteiro CM, Torocsik D, D'Avila H, Dezso B, et al. Mycobacterium bovis bacillus Calmette-Guerin infection induces TLR2-dependent peroxisome proliferator-activated receptor gamma expression and activation: functions in inflammation, lipid metabolism, and pathogenesis. J Immunol. 2009;183(2):1337-45. PubMed PMID: 19561094.
39. Li AC, Glass CK. The macrophage foam cell as a target for therapeutic intervention. Nat Med. 2002;8(11):1235-42. Epub 2002/11/02. doi: 10.1038/nm1102-1235. PubMed PMID: 12411950.
40. Eom M, Hudkins KL, Alpers CE. Foam cells and the pathogenesis of kidney disease. Curr Opin Nephrol Hypertens. 2015;24(3):245-51. Epub 2015/04/19. doi: 10.1097/MNH.0000000000000112. PubMed PMID: 25887903; PubMed Central PMCID: PMCPMC4466027.
41. Croze E, Yamaguchi KD, Knappertz V, Reder AT, Salamon H. Interferon-beta-1b-induced short- and long-term signatures of treatment activity in multiple sclerosis. Pharmacogenomics J. 2012. Epub 2012/06/20. doi: 10.1038/tpj.2012.27. PubMed PMID: 22711062.
42. Fuchs T, Hahn M, Ries L, Giesler S, Busch S, Wang C, et al. Expression of combinatorial immunoglobulins in macrophages in the tumor microenvironment. PLoS One. 2018;13(9):e0204108. Epub 20180921. doi: 10.1371/journal.pone.0204108. PubMed PMID: 30240437; PubMed Central PMCID: PMCPMC6150476.

Figure 1

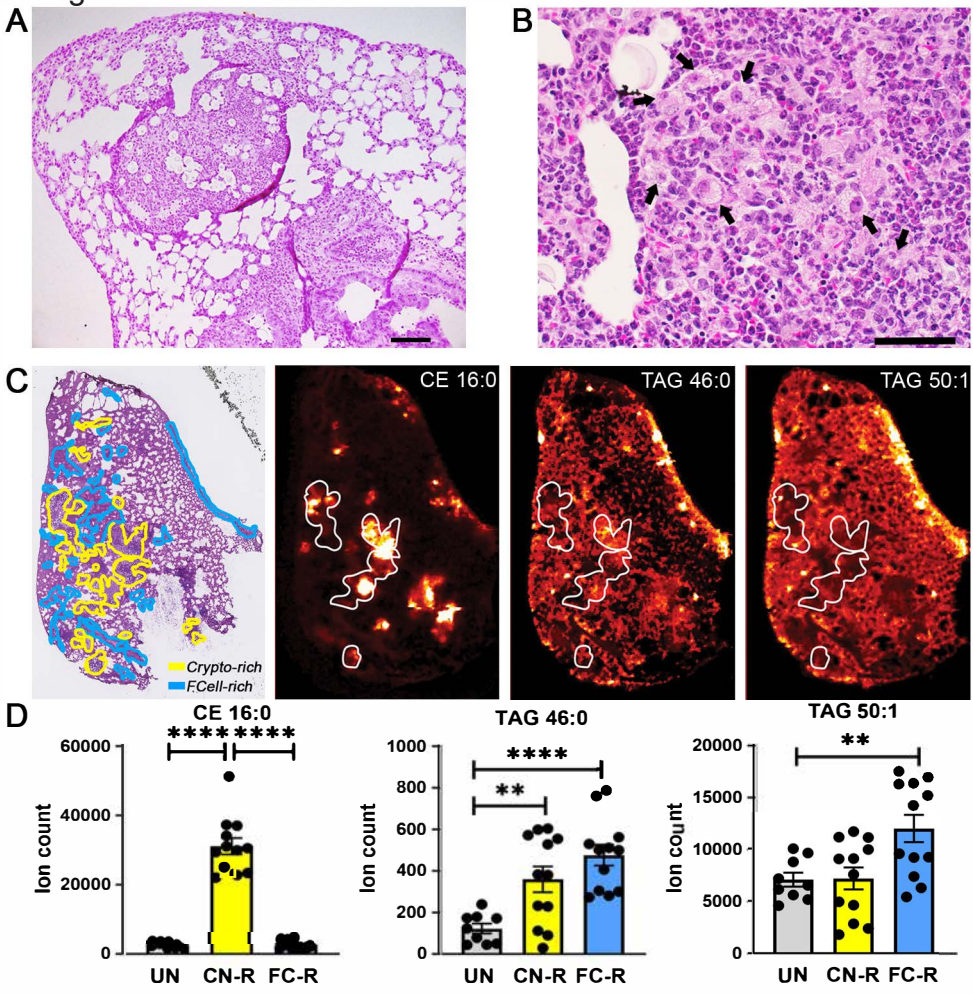
A
B
C
CE 16:0
TAG 46:0
TAG 50:1
Crypto-rich
FCell-rich
D
CE 16:0
TAG 46:0
TAG 50:1
Ion count
UN
CN-R
FC-R

Figure 2

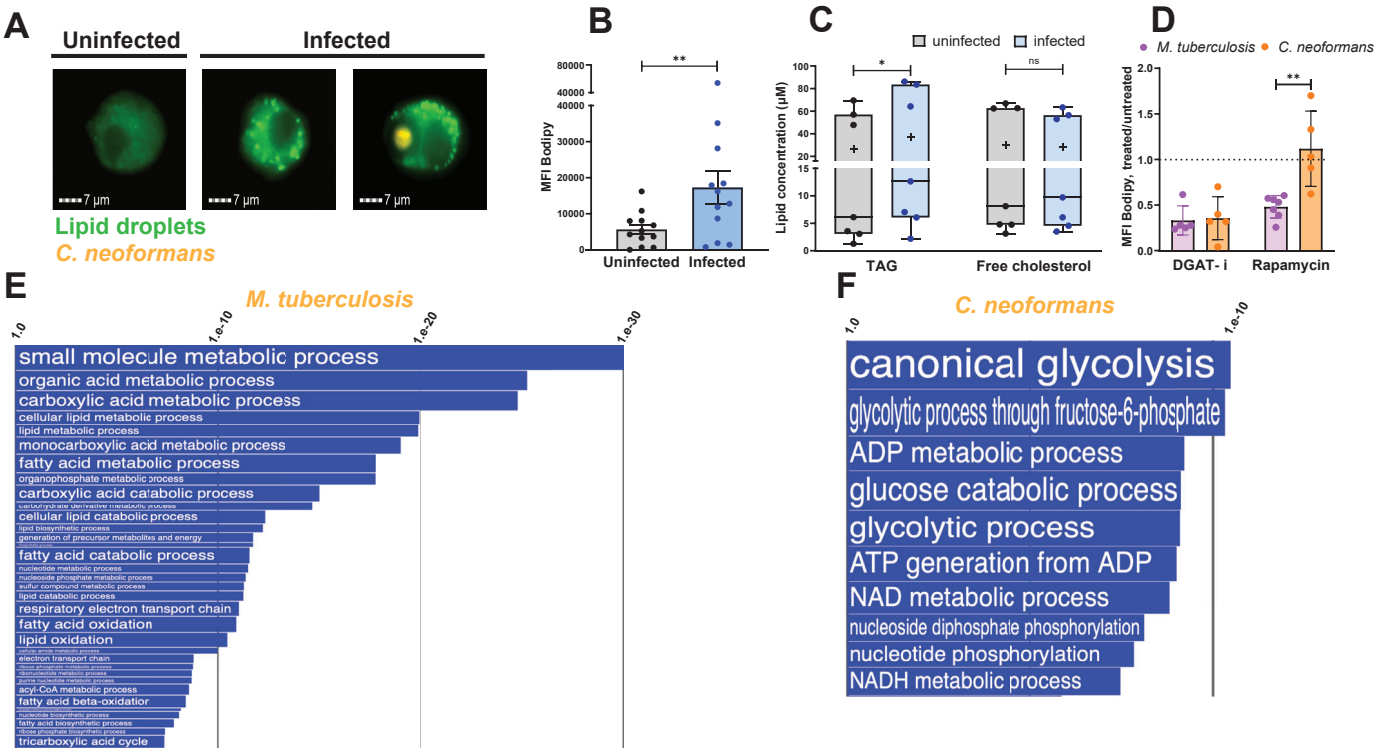
A
Uninfected
Infected
7 µm
7 µm
7 µm
Lipid droplets
C. neoformans
B
MFI Bodipy
Uninfected
Infected
C
uninfected
infected
Lipid concentration (µM)
TAG
Free cholesterol
D
M. tuberculosis
C. neoformans
MFI Bodipy, treated/untreated
DGAT- i
Rapamycin
E
M. tuberculosis
small molecule metabolic process
organic acid metabolic process
carboxylic acid metabolic process
cellular lipid metabolic process
lipid metabolic process
monocarboxylic acid metabolic process
fatty acid metabolic process
organophosphate metabolic process
carboxylic acid catabolic process
cellular lipid catabolic process
lipid biosynthetic process
generation of precursor metabolites and energy
fatty acid catabolic process
nucleotide metabolic process
nucleoside phosphate metabolic process
sulfur compound metabolic process
lipid catabolic process
respiratory electron transport chain
fatty acid oxidation
lipid oxidation
electron transport chain
acyl-CoA metabolic process
fatty acid beta-oxidation
nucleotide biosynthetic process
fatty acid biosynthetic process
tricarboxylic acid cycle
F
C. neoformans
canonical glycolysis
glycolytic process through fructose-6-phosphate
ADP metabolic process
glucose catabolic process
glycolytic process
ATP generation from ADP
NAD metabolic process
nucleoside diphosphate phosphorylation
nucleotide phosphorylation
NADH metabolic process

Figure 3

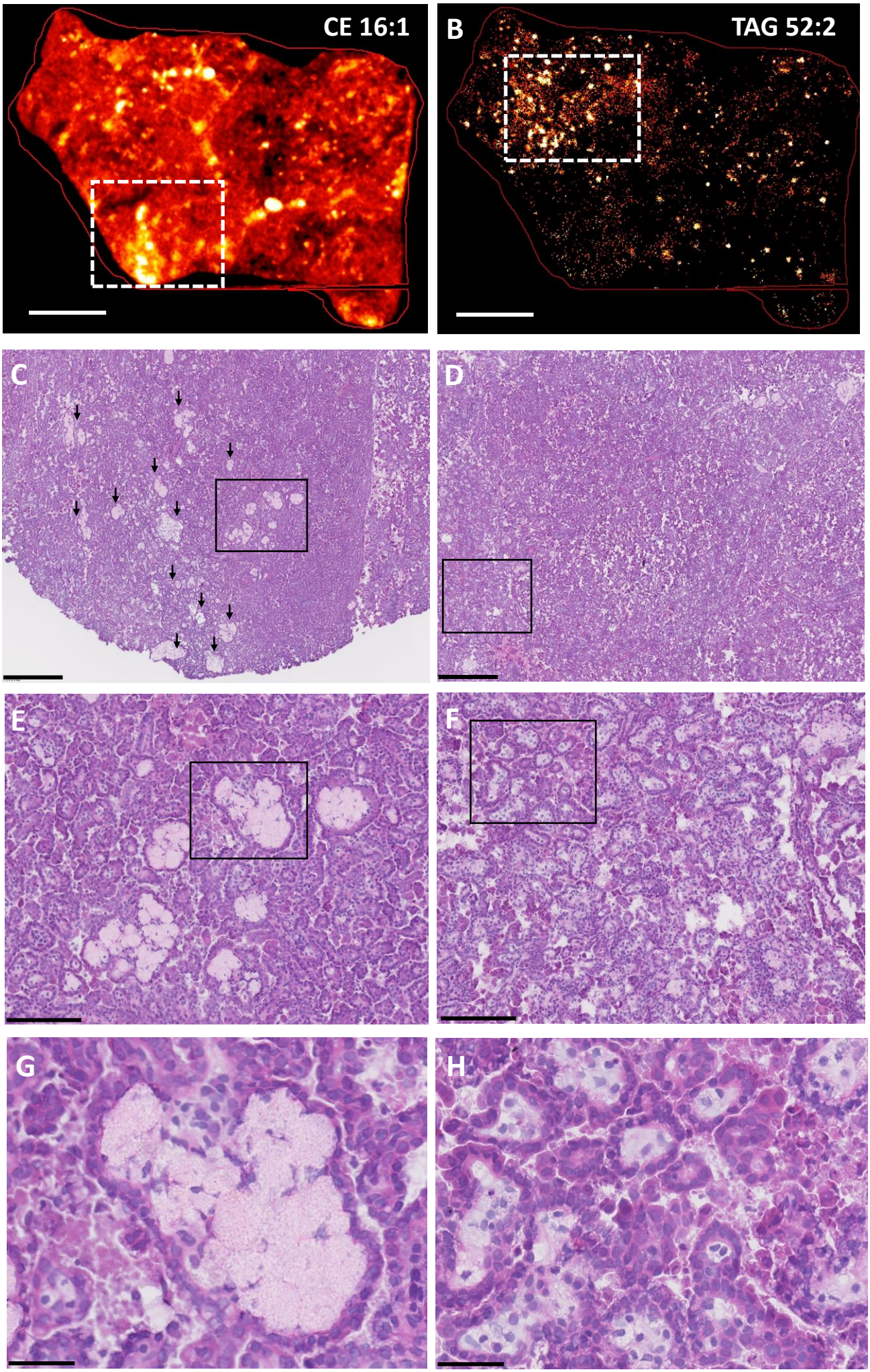

Figure 4

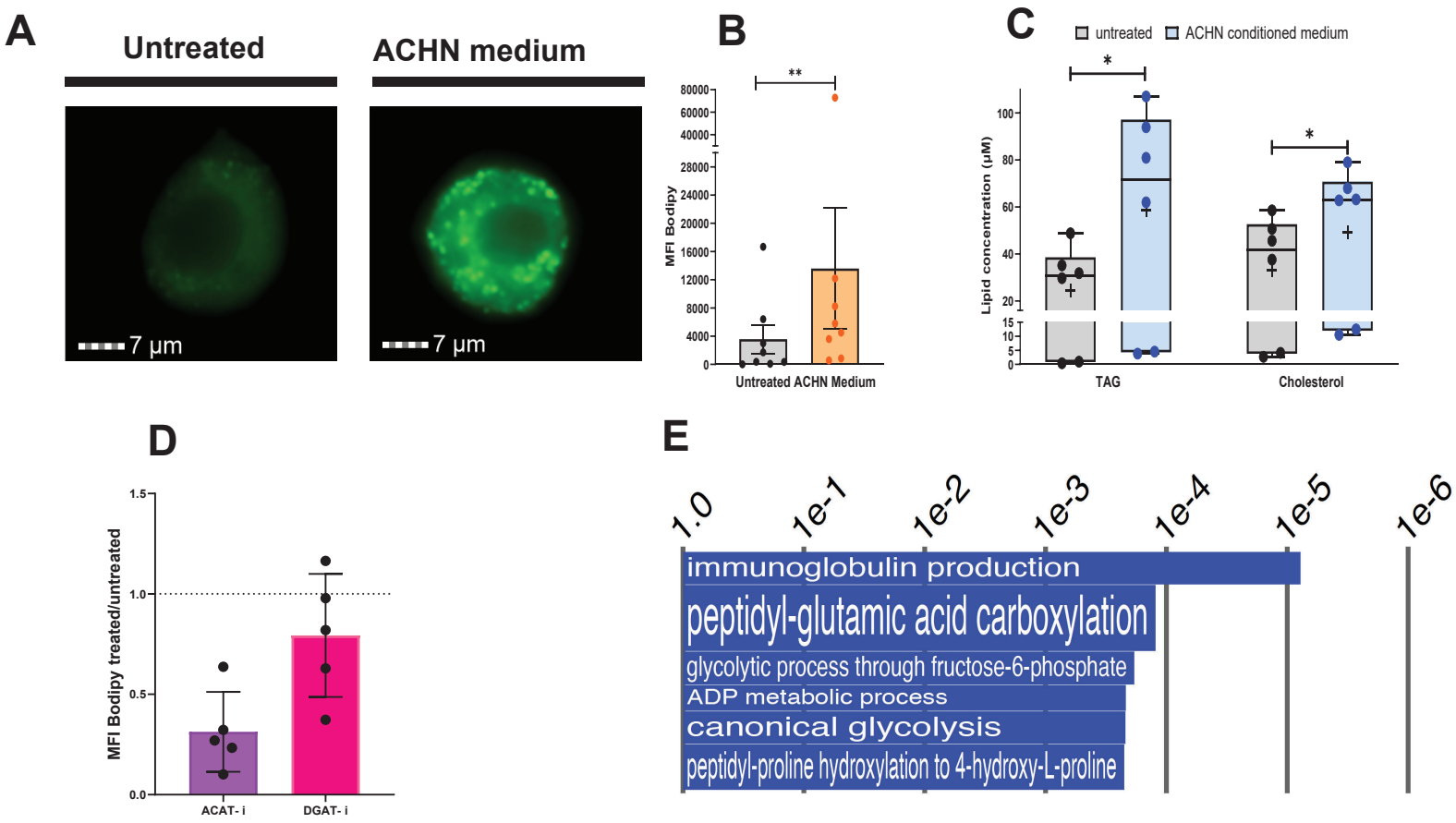
A
Untreated
ACHN medium
7 µm
7 µm
B
MFI Bodipy
Untreated ACHN Medium
C
untreated
ACHN conditioned medium
Lipid concentration (µM)
TAG
Cholesterol
D
MFI Bodipy treated/untreated
ACAT- i
DGAT- i
E
1.0
1e-1
1e-2
1e-3
1e-4
1e-5
1e-6
immunoglobulin production
peptidyl-glutamic acid carboxylation
glycolytic process through fructose-6-phosphate
ADP metabolic process
canonical glycolysis
peptidyl-proline hydroxylation to 4-hydroxy-L-proline

Supplementary Information

Heterogeneity of foam cell biogenesis across diseases

Valentina Guerrini[1*], Brendan Prideaux[2], Rehan Khan[1], Selvakumar Subbian[1], Yina Wang[3], Evita Sadimin[4*], Siddhi Pawar[3], Rahul Ukey[1], Eric A. Singer[4*], Chaoyang Xue[3], Maria Laura Gennaro[1**]

Supplementary Figures

Fig. S1. Low-magnification images of murine lungs uninfected and infected with *C. neoformans* H99.

Fig. S2. Hematoxylin-eosin staining and MALDI imaging of uninfected murine lung sections.

Fig. S3. Macrophage lipid droplet accumulation in response to infection with live *C. neoformans*, or treatment with cell-free fungal culture medium, or with heat-killed fungal cells.

Fig. S4. Metabolism-associated pathways (A) upregulated in *M. tuberculosis*-infected human monocyte-derived macrophages and (B) downregulated in *C. neoformans*-infected human monocyte-derived macrophages.

Fig. S5. Spatial distributions of cholesterol ester (CE) species in papillary renal cell carcinoma (pRCC) (Patient P1).

Fig. S6. Spatial distribution of triglyceride (TAG) species in papillary renal cell carcinoma (pRCC) (Patient P1).

Fig. S7. Spatial distribution of triglyceride (TAG) and cholesteryl ester (CE) species in papillary renal cell carcinoma biopsies collected from patients P2 and P3**.**

Fig. S8. Production of cytokines by human monocyte-derived macrophages treated with ACHN-conditioned culture medium and lipogenic effect of IL-8 at different concentrations.

Fig. S9. Metabolism-associated pathways downregulated in ACHN-medium-treated human monocyte-derived macrophages.

Supplementary Tables

Table S1. List of triglyceride and cholesteryl ester species detected in tissues by MALDI-MSI.

Table S2a. Top five down- and up-regulated genes in macrophages infected with *M. tuberculosis.*

Table S2b. Genes functionally related to top five down- and up-regulated genes in macrophages infected with *M. tuberculosis.*

Table S3a. Top five down- and up-regulated genes in macrophages infected with *C. neoformans.*

Table S3b. Genes functionally related to top five down- and up-regulated genes in macrophages infected with *C. neoformans.*

Table S4. Levels of cytokines in supernatants of ACHN cell cultures and MDM treated with ACHN-conditioned culture medium.

Table S5a. Top five down- and up-regulated genes in macrophages treated with ACHN-conditioned medium.

Table S5b. Genes functionally related to top five down- and up-regulated genes in macrophages treated with ACHN-conditioned culture medium.

Supplementary Text on transcriptomics analyses

Supplementary References

Supplementary Figures

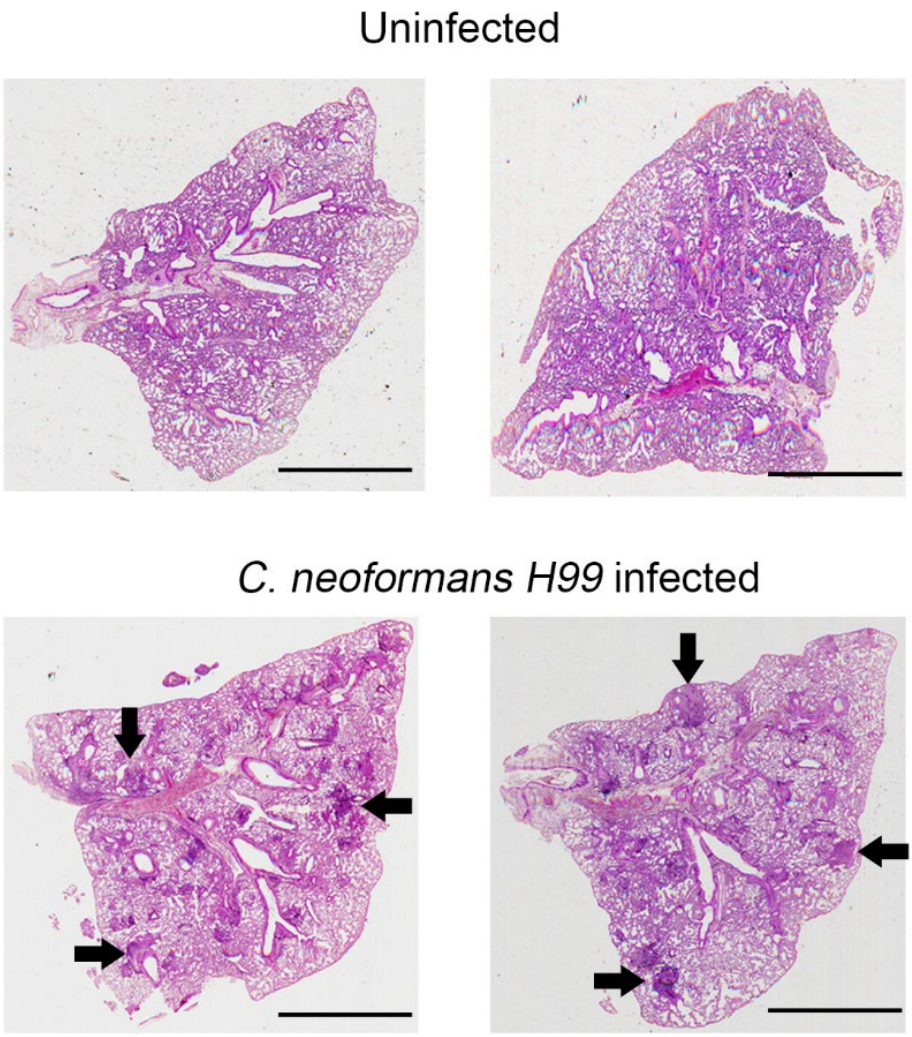

Supplementary Fig. S1. Low-magnification images of murine lungs uninfected and infected with *C. neoformans* H99. H&E staining of uninfected (top panels) and infected (bottom panels) lung sections. Black arrows show cellular aggregates in the infected tissue. Images were photographed at 20x magnification; scale bar is 2 mm.

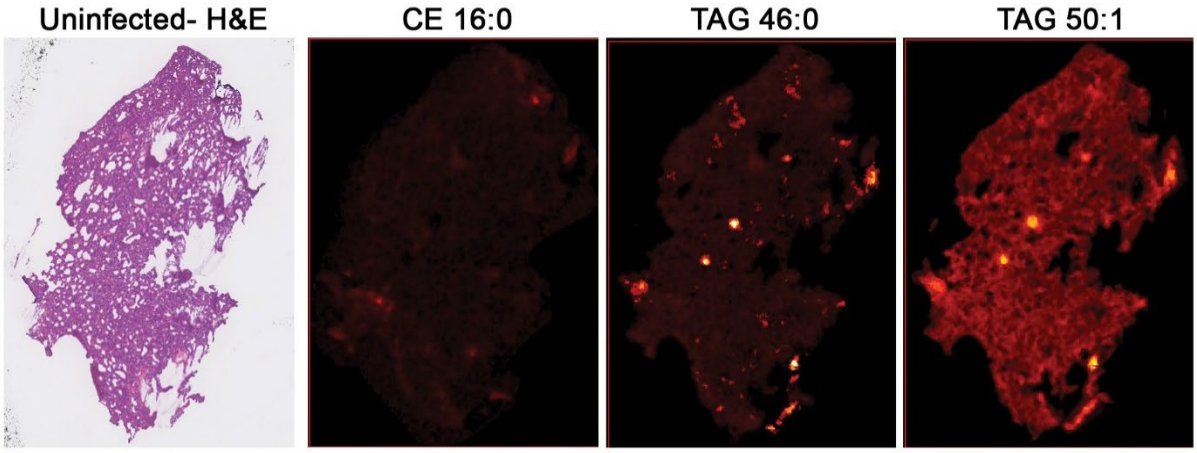

Supplementary Fig. S2. Hematoxylin-eosin staining and MALDI imaging of uninfected murine lung sections. The left panel shows H&E staining of uninfected lung sections. The three additional panels show MALDI imaging of storage lipids in lung sections contiguous to those used for H&E staining. Representative species are shown, CE (16:0) and TAG (46:0 and 50:1), corresponding to those shown in Fig. 1C (TAG and CE species detected are listed in **Table S1**).

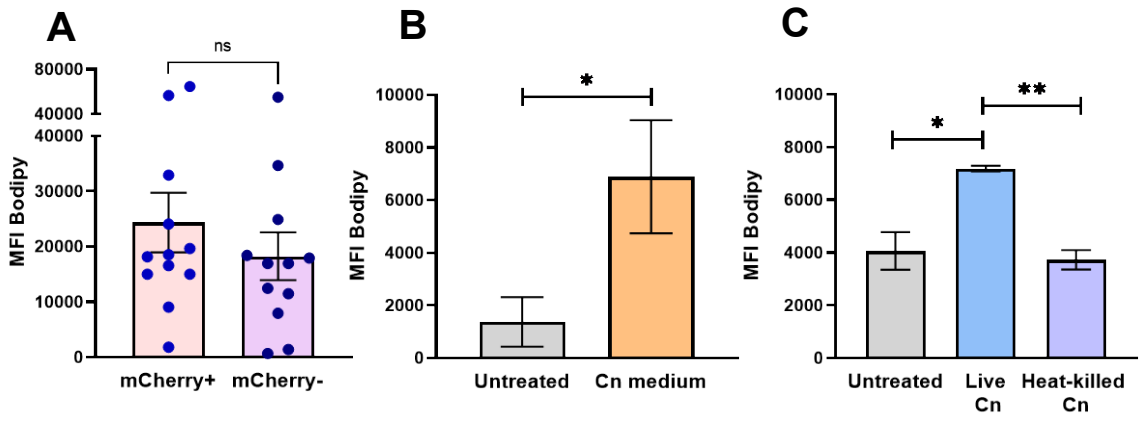

Supplementary Fig. S3. Macrophage lipid droplet accumulation in response to infection with live *C. neoformans*, or treatment with cell-free fungal culture medium, or with heat-killed fungal cells. In all panels, lipid droplet content of monocyte-derived macrophages (MDM) was measured by imaging flow cytometry and expressed as median fluorescence intensity (MFI) of Bodipy 493/503. **A.** MDM were infected with *C. neoformans* expressing mCherry and lipid droplet content was measured at 24 h post-infection in macrophages in the infected culture wells carrying or not carrying intracellular fungi (mCherry+ and mCherry-). Each dot represents one human donor. **B.** MDM were treated for 7 days with cell-free culture filtrate of *C. neoformans* grown in RPMI medium (Cn medium) or sterile RPMI medium (untreated). **C.** THP1 cells were treated with live or heat-killed *C. neoformans* (Cn) for 24 h. Statistics: mean and SEM (A-B) and mean and SD of triplicates (C-D) are shown; ns, non-significant; *, p <0.05; **, p <0.01 (paired t-test).

A. ***M. tuberculosis***

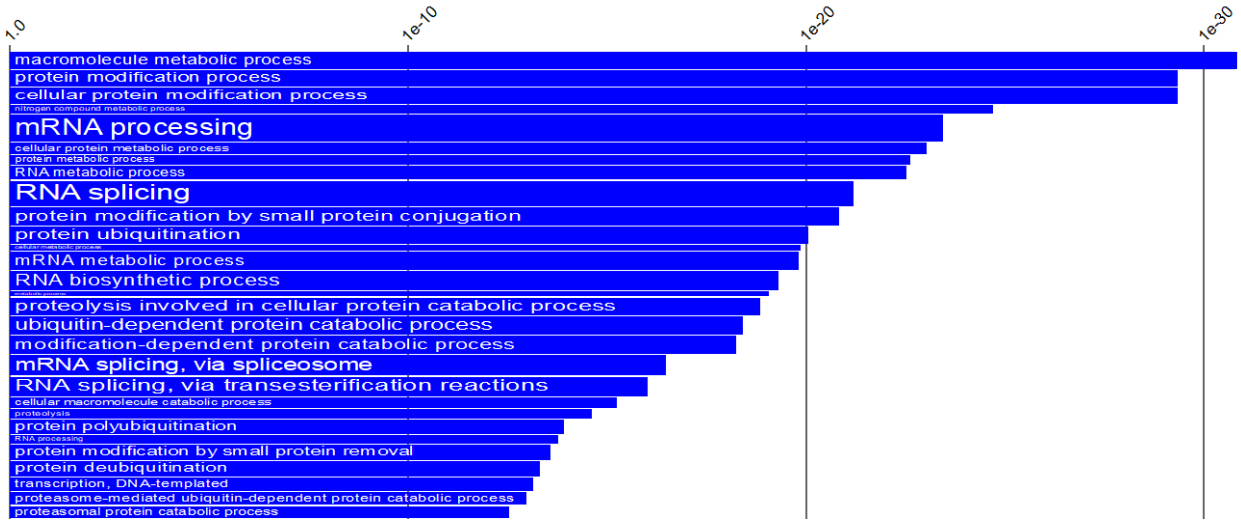

B. ***C. neoformans***

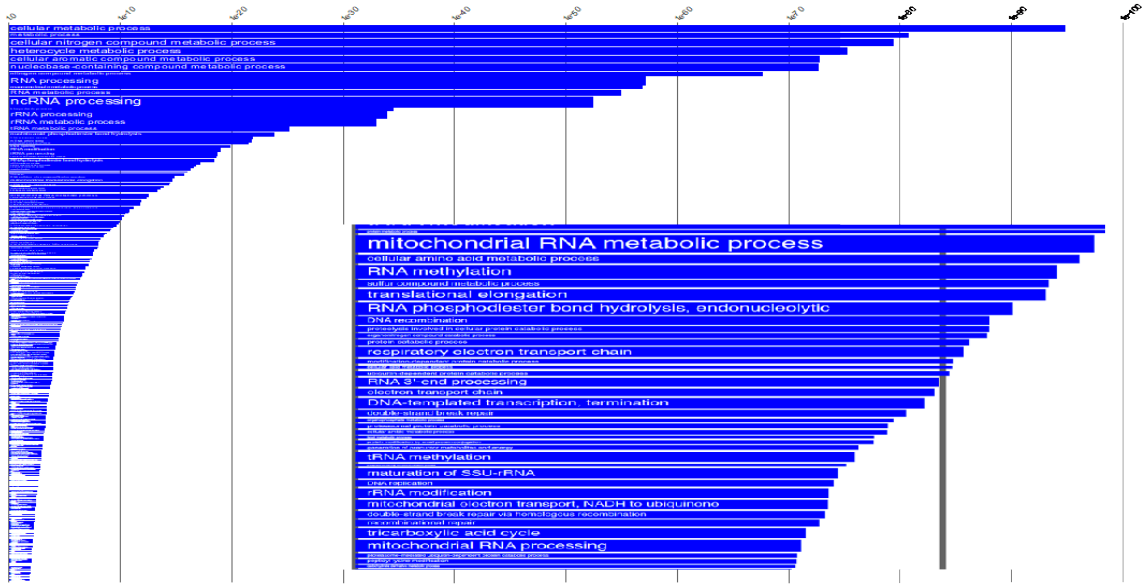

Supplementary Fig. S4. A. Upregulated metabolism-associated pathways in *M. tuberculosis*-infected human monocyte-derived macrophages. B. Downregulated metabolism-associated pathways in *C. neoformans*-infected human monocyte-derived macrophages. The panels show Gene Ontology (GO) annotations related to metabolic processes that were upregulated in *M. tuberculosis*-infected MDM and downregulated in *C. neoformans*-infected MDM, relative to uninfected control cells. The differential expression between sample classes (infected vs uninfected) was tested with coincident extreme ranks in numerical observations (CERNO). Pathways were selected using a cutoff false discovery rate of

0.05; the *p*-values for these pathways were plotted on the *x*-axis. To represent effect size, pathway gene sets containing fewer genes were given greater bar height/font size than were larger sets that yielded similar *p* values. For visualization purposes, panel A shows top-ranking annotations, and panel B. contains an inset highlighting mitochondria-related annotations.

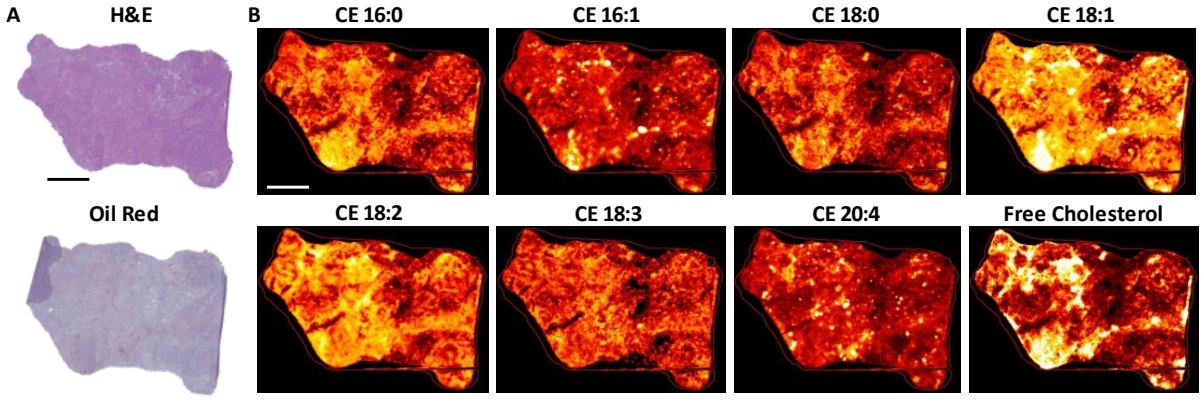

Supplementary Fig. S5. Spatial distribution of cholesterol ester (CE) species in papillary renal cell carcinoma (pRCC) (patient P1). A. Hematoxylin-eosin- and oil-red-stained kidney sections contiguous to those used for MALDI imaging. **B.** MALDI-2-MSI signal distribution for the major detected cholesterol ester species. Scale bar = 5 mm

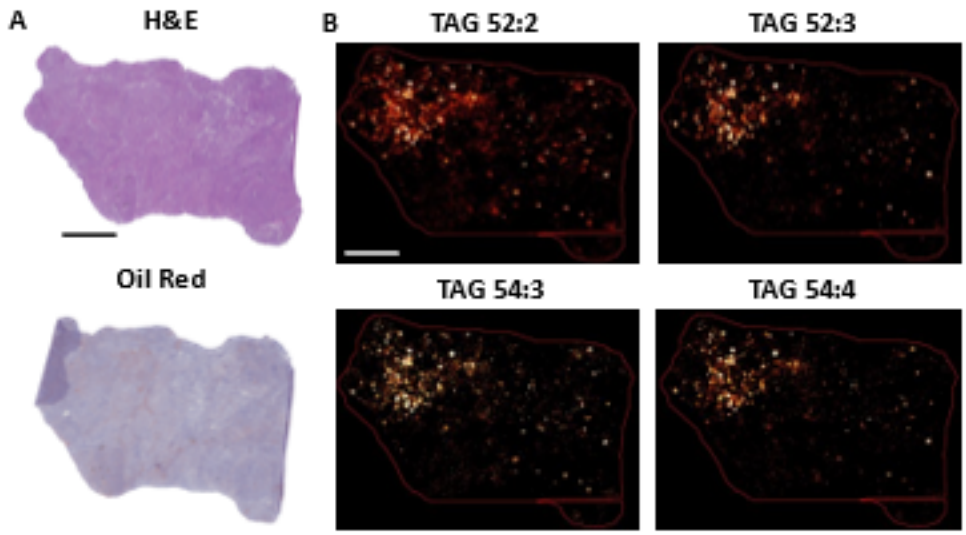

Supplementary Fig. S6. Spatial distribution of triglyceride (TAG) species in papillary renal cell carcinoma (pRCC) (patient P1). A. Hematoxylin-eosin- and oil-red-stained kidney sections contiguous to those used for MALDI imaging. **B.** MALDI-2-MSI signal distribution for four of the major detected TAG species. Scale bar = 5 mm

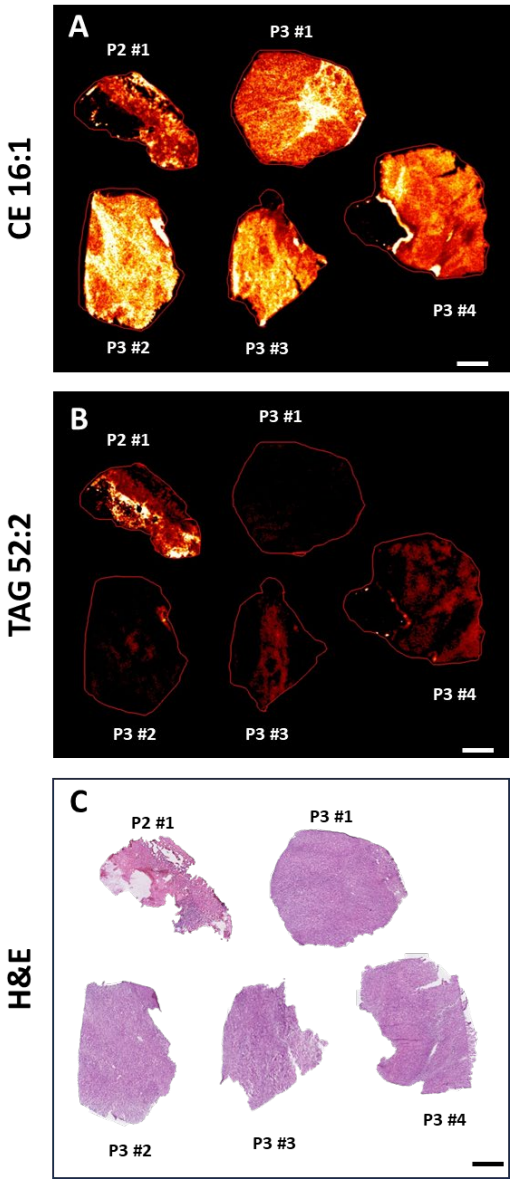

Supplementary Fig. S7 Spatial distribution of triglyceride (TAG) and cholesteryl ester (CE) species in papillary renal cell carcinoma biopsies collected from patients P2 and P3. A. MALDI-2-MSI signal distribution for CE 16:1. **B.** MALDI-2-MSI signal distribution for TAG 52:2. C. Hematoxylin-eosin-stained kidney sections contiguous to those used for MALDI imaging. P = patient ID, # = biopsy number. Scale bar = 5 mm

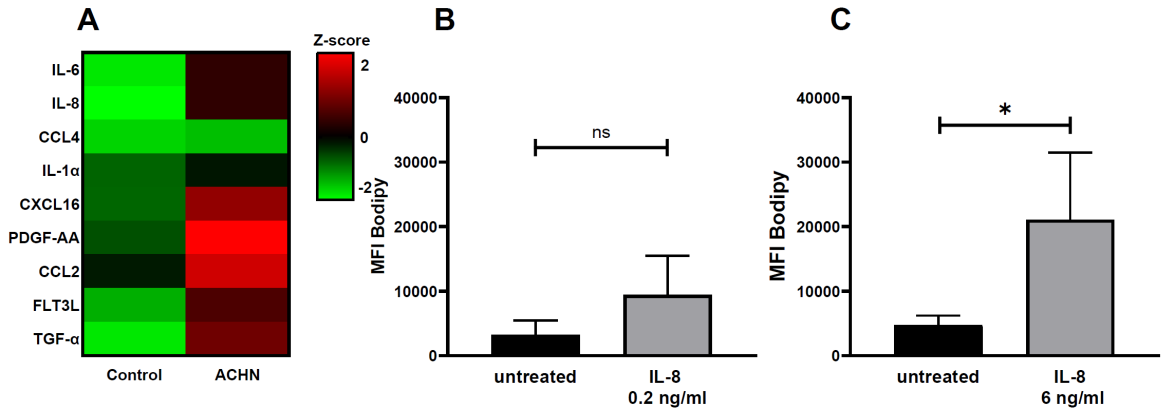

Supplementary Fig. S8. Production of cytokines by human monocyte-derived macrophages treated with ACHN-conditioned culture medium and lipogenic effect of IL-8 at different concentrations. A. The heat map shows cytokines and chemokines differentially expressed by MDM exposed to conditioned medium from ACHN cell cultures relative to control, untreated MDM, as described in Fig. 4. Cytokines/chemokines were measured as technical duplicates using a 43-plex array and Luminex technology. The average *Z*-score for five donors was calculated for each analyte. Color gradient from green to red represents increasing concentrations. Data shown had $p < 0.05$ (paired *t*-test). **B-C.** Lipid droplet content of MDM was measured as median fluorescence intensity (MFI) of Bodipy 493/503 by imaging flow cytometry, following 7-day treatment with recombinant IL-8, at two different concentrations, as indicated. Statistics: mean and SD of triplicate measurements (B) and mean and SEM of multiple donors (C) are shown; ns, non-significant; *, $p < 0.05$ (B, unpaired *t*-test; C, Mann-Whitney test).

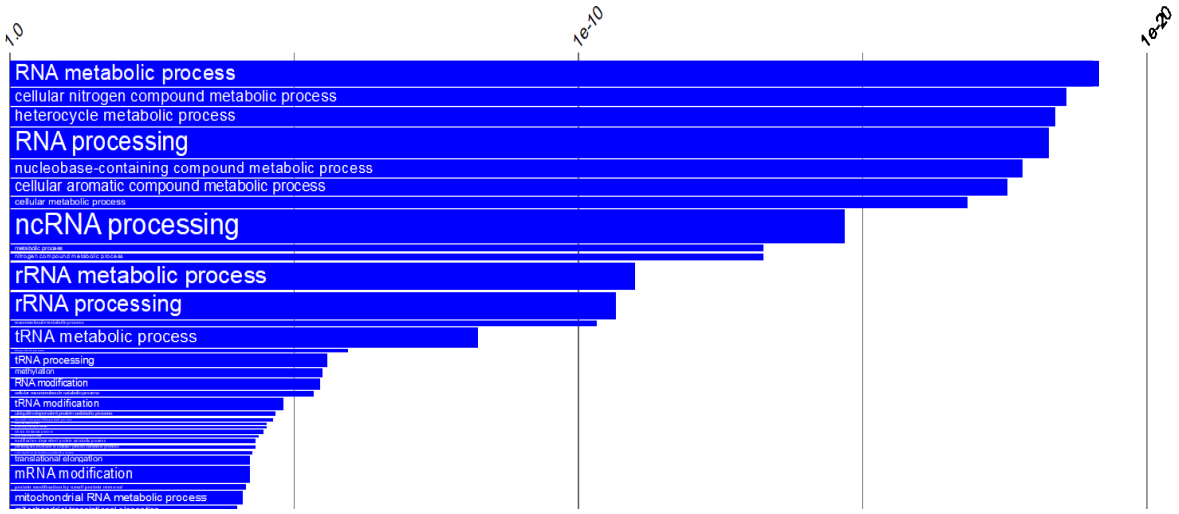

Supplementary Fig. S9. Downregulated metabolism-associated pathways in ACHN-medium-treated human monocyte-derived macrophages. The figure shows Gene Ontology (GO) annotations related to metabolic processes that were downregulated in MDM treated with ACHN conditioned medium, relative to untreated control cells. The differential expression between sample classes (treated vs untreated) was tested and selected pathways were represented as described in Figure S4. For visualization purposes, top-ranking annotations are shown.

Supplementary Tables

Supplementary Table S1. List of triglyceride and cholesteryl ester species detected in tissues by MALDI-MSI.

TAG	Detected in *Cryptococcus*	Detected in pRCC	CE	Detected in *Cryptococcus*	Detected in pRCC
Species	Tissue	Tissue	Species	Tissue	Tissue
48:0	✓	×	16:0	✓	✓
48:1	✓	×	16:1	✓	✓
48:2	✓	×	18:0	✓	✓
48:3	✓	×	18:1	✓	✓
50:0	✓	×	18:2	✓	✓
50:1	✓	✓	18:3	✓	✓
50:2	✓	✓	20:1	✓	✓
50:3	✓	✓	20:2	×	✓
50:4	✓	×	20:4	✓	✓
52:1	✓	×			
52:2	✓	✓			
52:3	✓	✓			
52:4	✓	✓			
52:5	✓	✓			
52:6	✓	×			
54:2	✓	✓			
54:3	✓	✓			
54:4	✓	✓			
54:5	✓	✓			
54:6	✓	×			
54:7	✓	×			
56:3	✓	×			
56:4	✓	×			

Triglyceride (TAG) species (identified by the total number of carbons and double bonds in the esterified fatty acids) and cholesteryl ester (CE) species detected by MALDI-MSI in the cryptococcus-infected lung tissues and papillary renal cell carcinoma (pRCC) tissue. ✓, detected; x, not detected.

Supplementary Table S2a. Top five down- and up-regulated genes in macrophages infected with *M. tuberculosis.*

Gene ID	Gene	log2FoldChange	*p* value
ENSG00000005469	CROT	-0.694245982	6.81E-10
ENSG00000183549	ACSM5	-1.875070163	2.15E-12
ENSG00000072210	ALDH3A2	-0.675169083	1.18E-15
ENSG00000131238	PPT1	-0.769679647	6.47E-16
ENSG00000168765	GSTM4	-0.846851963	4.64E-14
ENSG00000105325	FZR1	0.451795	1.01E-10
ENSG00000186187	ZNRF1	0.884946	4.79E-17
ENSG00000108306	FBXL20	0.849817	9.11E-17
ENSG00000186591	UBE2H	0.795385	3.10E-25
ENSG00000187555	USP7	0.206178	4.81E-06

Genes in differentially expressed metabolism-related Gene Ontology gene sets having FDR < 0.05 were selected based on individual *p* value ($p << 0.05$) and ranked by log2 fold change (infected vs non-infected) and number of occurrences in the differentially expressed gene sets. The top five down- and up-regulated genes were selected for further analysis.

Supplementary Table S2b. Genes functionally related with the top five down- and up-regulated genes in macrophages infected with *M. tuberculosis*.

Gene ID	Gene	log2FoldChange	*p* value
ENSG00000215009	ACSM4	-1.65627	2.66E-05
ENSG00000130377	ACSBG2	-1.09841	3.99E-03
ENSG00000140284	SLC27A2	0.929524	2.40E-03
ENSG00000143554	SLC27A3	0.440446	2.69E-02
ENSG00000110090	CPT1A	-0.69747	6.60E-05
ENSG00000157184	CPT2	-0.32849	3.84E-05
ENSG00000154227	CERS3	1.207873	6.71E-03
ENSG00000139624	CERS5	0.437953	5.94E-06
ENSG00000177076	ACER2	-0.46598	2.77E-02
ENSG00000141510	TP53	-0.34037	1.19E-04
ENSG00000109670	FBXW7	0.514687	0.00000987
ENSG00000135679	MDM2	0.745793	1.91E-10
ENSG00000100219	XBP1	1.329735	1.36E-11
ENSG00000155792	DEPTOR	-2.04205	0.0000007
ENSG00000164181	ELOVL7	4.018986	1.04E-33
ENSG00000175445	LPL	-1.17544	6.57E-08
ENSG00000134184	GSTM1	-0.95459	0.000000069
ENSG00000213366	GSTM2	-1.23318	0.000000626
ENSG00000166851	PLK1	-1.07326	0.0025
ENSG00000092964	DPYSL2	-0.9294	1.38E-06
ENSG00000013588	GPRC5A	6.429513	2.92E-81
ENSG00000181773	GPR3	3.096538	1.07E-34
ENSG00000183484	GPR132	3.238435	2.91E-26
ENSG00000180758	GPR157	2.357273	5.3E-21
ENSG00000173698	GPR64	2.313555	8.38E-17
ENSG00000139572	GPR84	2.131323	4.78E-10
ENSG00000182885	GPR97	2.623284	1.95E-09
ENSG00000188316	ENO4	-1.32246	7.67E-07
ENSG00000077721	UBE2A	0.552901	1.40E-08
ENSG00000160087	UBE2J2	0.405355	2.54E-08
ENSG00000177889	UBE2N	0.348958	3.68E-08
ENSG00000131508	UBE2D2	0.331604	7.16E-07
ENSG00000185651	UBE2L3	0.381012	3.78E-06
ENSG00000160714	UBE2Q1	0.35768	2.01E-05
ENSG00000072401	UBE2D1	0.867935	3.27E-05

ENSG00000104343	UBE2W	0.503851	4.69E-05
ENSG00000182247	UBE2E2	0.746942	0.000065
ENSG00000078140	UBE2K	0.277765	0.000104
ENSG00000170142	UBE2E1	0.523719	0.000327
ENSG00000156587	UBE2L6	1.059927	0.000437
ENSG00000175931	UBE2O	0.349526	0.000465
ENSG00000130725	UBE2M	0.31568	0.000899
ENSG00000107341	UBE2R2	0.236068	0.002875
ENSG00000184182	UBE2F	0.245525	0.021078
ENSG00000198833	UBE2J1	0.305753	0.02493
ENSG00000187531	SIRT7	0.5201	1.33E-10
ENSG00000177463	NR2C2	0.771918	0.000254
ENSG00000182054	IDH2	-0.83851	2.92E-14
ENSG00000138413	IDH1	-0.94364	2.62E-18
ENSG00000142208	AKT1	-0.16012	0.045604
ENSG00000082701	GSK3B	0.515329	0.000158

Differentially expressed genes ($p < 0.05$) reported in the published literature as functionally related to the top five up- and down-regulated genes in Table S2a.

Supplementary Table S3a. Top five down- and up-regulated genes in macrophages infected with *C. neoformans.*

Gene	Gene Id	log2FoldChange	*p* value
ENSG00000116750	UCHL5	-0.20727	0.04472
ENSG00000138035	PNPT1	-0.54945	1.67E-10
ENSG00000130348	QRSL1	-0.37168	3.88E-07
ENSG00000196510	ANAPC7	-0.39341	0.000302
ENSG00000131467	PSME3	-0.30045	3.30E-05
ENSG00000109107	ALDOC	1.825971589	2.32E-10
ENSG00000111674	ENO2	1.489680497	9.70E-15
ENSG00000159399	HK2	1.121945578	6.74E-16
ENSG00000102144	PGK1	0.746990585	2.14E-08
ENSG00000111640	GAPDH	0.713009241	1.06E-07

Gene identification for gene-level analysis was performed as in Table S2a.

Supplementary Table S3b. Genes functionally related with the top five down- and up-regulated genes in macrophages infected with *C. neoformans.*

Gene	Gene Id	log2FoldChange	*p* value
ENSG00000185920	PTCH1	0.761480524	0.012629752
ENSG00000127528	KLF2	0.62022683	0.047195731
ENSG00000166819	PLIN1	0.973316711	0.003288899
ENSG00000147872	PLIN2	0.692199046	0.00059194
ENSG00000149925	ALDOA	0.568357915	4.63E-06
ENSG00000111669	TPI1	0.6108752	5.94E-07
ENSG00000171314	PGAM1	0.429844596	0.001449782
ENSG00000105220	GPI	0.684479515	7.26E-09
ENSG00000067057	PFKP	0.690877949	0.000281329
ENSG00000152256	PDK1	1.070412291	8.18E-08
ENSG00000067992	PDK3	0.363881857	0.004868894
ENSG00000134333	LDHA	1.050510273	3.90E-08
ENSG00000104812	GYS1	0.794960339	3.17E-07
ENSG00000174437	ATP2A2	-0.330898147	0.029025124
ENSG00000132356	PRKAA1	-0.186245418	0.045627492
ENSG00000131828	PDHA1	-0.222577362	0.025045384
ENSG00000072210	ALDH3A2	-0.331695382	7.63E-05
ENSG00000161618	ALDH16A1	-0.281990927	0.008872148
ENSG00000184254	ALDH1A3	-0.998071894	0.011142259
ENSG00000159423	ALDH4A1	-0.573208906	0.013428796
ENSG00000137124	ALDH1B1	-0.500558706	0.026687482
ENSG00000135218	CD36	-0.435604275	0.045176474

Differentially expressed genes ($p < 0.05$) reported in the published literature as functionally related to the top five up- and down-regulated genes in Table S3a.

Supplementary Table S4. Levels of cytokines in supernatants of ACHN cell cultures and MDM treated with ACHN-conditioned culture medium.

Cytokine	ACHN (pg/ml)	ACHN-medium treated MDM (pg/ml)
IL-6	174	82
IL-8	543	4889
CCL4	137	2414
IL-1α	4	34
CXCL16	23	1898
PDGF-AA	46	37
CCL2	405	13775
FLT3L	10	22
TGF-α	6	17

The level of cytokines produced by ACHN cell cultures was calculated as average of technical duplicates for each analyte. MDM from donors (n=5) was treated with ACHN-conditioned culture medium. The average level in MDM supernatants from the five donors was calculated for each analyte.

Supplementary Table S5a. Top five down and upregulated genes in macrophages treated with ACHN-conditioned culture medium.

Gene	Gene Id	log2FoldChange	*p* value
ENSG00000109819	PPARGC1A	-1.108179567	0.0019129
ENSG00000179598	PLD6	-0.340258537	0.0313289
ENSG00000164742	ADCY1	-1.789945859	1.59E-05
ENSG00000156239	N6AMT1	-0.407562926	0.0036691
ENSG00000215009	ACSM4	-0.732880759	0.0301056
ENSG00000111674	ENO2	0.585748	0.005669
ENSG00000160883	HK3	0.417557	0.035561
ENSG00000111669	TPI1	0.280168	0.035629
ENSG00000102144	PGK1	0.263218	0.041578
ENSG00000162433	AK4	0.550335	0.00025

Gene identification for gene-level analysis was performed as in Table S2a.

Supplementary Table S5b. Genes functionally related with the top five down and upregulated genes in macrophages treated with ACHN conditioned culture medium.

Gene	Gene Id	log2FoldChange	*p* value
ENSG00000135218	CD36	-0.71398	0.002177
ENSG00000166411	IDH3A	-0.36846	0.012774
ENSG00000110090	CPT1A	-0.3713	0.048744
ENSG00000165092	ALDH1A1	-0.6716	0.005934
ENSG00000214456	PLIN5	0.763578	0.033995
ENSG00000007866	TEAD3	0.442895	0.043061
ENSG00000142583	SLC2A5	0.948899	0.001353
ENSG00000114268	PFKFB4	0.682204	3.73E-05

Differentially expressed genes ($p < 0.05$) reported in the published literature as functionally related to the top five up- and down-regulated genes in Table S5a.

Supplementary text on transcriptomics analyses

1. Metabolism-related gene-level analysis of *M. tuberculosis*-infected monocyte-derived macrophages.

Genes in differentially expressed metabolism-related Gene Ontology gene sets having FDR < 0.05 were selected based on individual *p* value ($p << 0.05$) and ranked by log2 fold change (infected vs non-infected) and number of occurrences in the differentially expressed gene sets. We analyzed the top five down- and up-regulated genes (**Table S2a**) and differentially expressed genes ($p < 0.05$) that were functionally related to them (**Table S2b**). In the text below, and in the subsequent sections, the names of the top five up- and down-regulated genes (**Table S2a**) are shown in bold. The names of the up- and down-regulated functionally related genes (**Table S2b**) are underlined.

Multiple mechanisms of decreased fatty acid oxidation were identified. These included downregulation of genes involved in (i) synthesis of acyl-CoA (acyl-CoA synthases <u>ACSM4</u>, **ACSM5**, <u>ACSBG2</u>), (ii) acyl-CoA conversion to acyl-carnitine [(carnitine transferase in peroxisome (**CROT**) and mitochondria (<u>CPT1A</u>, <u>CPT2</u>)], which is required for transport across the mitochondrial membrane (*1-3*), and (iii) oxidation to fatty acids of fatty aldehydes and fatty alcohols derived from lipid catabolism (fatty aldehyde dehydrogenase, **ALDH3A2**) (*4-6*).

Gene expression markers of increased production of triacylglycerols (TAG) were also identified. One set of gene expression changes were associated with increased production of ceramide, which induces triglyceride production (*7-10*). These included (i) downregulation of the aldehyde hydrogenase **ALDH3A2**, which converts hexadecenal to hexadecenoic acid. The resulting hexadecenal accumulation may lead to ceramide production; (ii) downregulation of ceramidase <u>ACER2</u>, and (iii) upregulation of ceramide synthases (<u>CERS3</u> and <u>CERS5</u>). An additional marker of triglyceride accumulation was the downregulation of the gene encoding palmitoyl-protein thioesterase 1 (**PPT1**), which expresses lipolytic activity (*11, 12*). TAG accumulation in *M. tuberculosis*-infected macrophages may also result from altered cellular redox. For example, we observed downregulation of genes encoding glutathione S-Transferase Mu (<u>GSTM1</u>, <u>GSTM2</u>, **GSTM4**), a scavenger of reactive oxygen species (ROS), which can induce lipid droplet formation by inducing the ASK1/p38/JNK pathway (*13-15*).

As mentioned in the main text, *M. tuberculosis*-infected macrophages exhibited downregulated TP53 gene and upregulated TP53-specific E3 ligases (FBXW7, MDM2) that target this factor for proteasomal degradation (*16-18*). Upregulation of XBP1 can also lead to decreased TP53 levels by inducing MDM2 (*19*). Reduced TP53 activity well correlates with downregulation of TP53-dependent Deptor, which negatively regulates mTOR (*20, 21*). mTORC1 signaling is lipogenic in multiple ways, including increased de novo lipid synthesis, reduced lipolysis, and reduced fatty acid oxidation (*22, 23*).

We also observed upregulation of metabolism-related ubiquitination processes, which was prominent both at the pathway- arufnd at the gene-level (**Fig. S4** and **Table S2a**). At the gene level, the top five upregulated genes featured genes encoding E3 ligases (**ZNRF1**) and associated proteins (**FZR1**, **FBXL20**, **UBE2H**) and the deubiquitinase **USP7,** which increases ZNRF1 activity as well as MDM2 activity (*24-29*). These changes presumably result in substantial macrophage proteome remodeling in response to *M. tuberculosis* infection. In particular, they may affect a variety of lipid metabolism regulators, including AKT1 and PLK1 (*30, 31*). **USP7** also stabilizes sirtuins (e.g., SIRT7, which is also upregulated at the gene level), resulting in increased expression of factors associated with TAG synthesis (*24, 32*).

2. Metabolism-related gene-level analysis of *C. neoformans*-infected monocyte-derived macrophages.

The top five up- and down-regulated genes (**Table S3a**) and functionally related, differentially expressed genes (**Table S3b**) were determined as described above for *M. tuberculosis* infection.

The top five upregulated genes encode glycolytic enzymes, strongly indicating a prominent role of a switch to glycolysis in *C. neoformans*-infected macrophages, which leads to increased triglyceride biosynthesis in multiple ways. Increased expression of hexokinase 2 (**HK2**) and other glycolytic enzymes (GPI, PFKP) results in increased production of fructose 1,6-bisphosphate, which can be converted to dihydroxyacetone phosphate (DHAP) and glyceraldehyde 3-phosphate (G3P), due to the increased production of aldolases (**ALDOC**, ALDOA). Also, the upregulation of the triosephosphate isomerase-encoding gene (TPI) might lead to increased production of DHAP, which is a precursor for triglyceride biosynthesis. The upregulation of additional glycolytic genes (**GAPDH**, **PGK1**, PGAM1, **ENO2**) might result in increased synthesis of phosphoenolpyruvate (PEP) (*33*). Increased PEP levels might inhibit

sarco/endoplasmic reticulum Ca2+-ATPase, resulting in calcium imbalance and endoplasmic reticulum stress, which ultimately lead to lipogenesis (*34-36*). Moreover, the products of glycolytic genes may favor lipid accumulation in ways other than their direct role in glycolysis. For example, the **HK2** product participates in the metabolic switch from oxidative phosphorylation to glycolysis (*37*) and inhibits lipases (*38*). In addition, phosphoglycerate kinase 1 (**PGK1**) can phosphorylate pyruvate dehydrogenase kinases, which are also upregulated (PDK1, PDK3), and inhibit the pyruvate dehydrogenase (PDH) complex (*39*). Inhibition of the PDH Complex, further compounded by the downregulation of one of its subunit-encoding genes (PDHA1), leads to impaired tricarboxylic acid cycle and enhanced glycolysis (*40*). As a result, pyruvate may accumulate and converted to lactate by lactate dehydrogenase (LDHA) (*41*), which we find upregulated. Lactate may inhibit lipolysis, thus resulting in lipid accumulation (*42*).

As mentioned in the main text, we also found indicators of reduced mitochondrial functions in *C. neoformans*-infected macrophages, including downregulation of polyribonucleotide nucleotidyl transferase 1 (**PNPT1**) and a glutaminyl-tRNA amidotransferase subunit 1 (**QRSL1**). The **PNPT1** product regulates the expression of the electron transport chain components at the mRNA and protein levels. Thus, downregulation of this gene might result in reduced function of the respiratory chain and decreased oxidative phosphorylation, leading to lipid accumulation (*43, 44*). The **QRSL1** product enables glutaminyl-tRNA synthase (glutamine-hydrolyzing) activity in the mitochondria. Missense mutations in the human QRSL1 locus have been associated with defects in mitochondrial respiratory chain complex and oxidative phosphorylation (*45, 46*). The resulting oxidative stress enhances lipogenesis (*47, 48*).

Lipid accumulation in *C. neoformans*-infected macrophages may also result from dysregulation of various other cellular activities. First, infected cells may exhibit increased fatty acid synthesis and decreased fatty acid oxidation due to the downregulation of (i) AMP-activated protein kinase (AMPK/PRKAA1), which inhibits de novo biosynthesis of fatty acids, increases fatty acid uptake, and stimulates fatty acid oxidation (*49-51*) and (ii) multiple genes encoding aldehyde dehydrogenases (ALDH3A2, ALDH16A1, ALDH1A3, ALDH4A1, ALDH1B1), which are involved in fatty acid oxidation (*6*). Second, perilipin genes (PLIN1, PLIN2), which are structural components of lipid droplets (*52*), are upregulated. PLIN gene upregulation may be associated, at least in part, with the downregulation of proteasome activator subunit 3 (**PSME3**) (*53*). The PSME3 product induces the degradation of Kruppel Like Factor 2 (KLF2) (*54*). Since KLF2 promotes the transcription of TAG synthesis and lipid storage genes, including PLIN1 and PLIN2 (*55*), increased KLF2 activity secondary to PSME3 downregulation is associated with lipid

accumulation (*56*). Third, one may hypothesize that another system involved in *C. neoformans*-infection-induced lipid accumulation is Hedgehog signaling. Inhibition of Hedgehog signaling results in fat accumulation (*57, 58*). Downregulation of ubiquitin C-terminal hydrolase L5 (**UCHL5**), which positively regulates Hedgehog signaling by deubiquitinating one of its components, the Smoothened (SMO) protein (*59, 60*), might result in reduced Hedgehog signaling and increased lipid accumulation. The observed upregulation of patched1 (PTCH1), which represses SMO (*61, 62*), is consistent with a role of Hedgehog in lipid accumulation in *C. neoformans*-infected macrophages. Fourth, the downregulation of anaphase promoting complex subunit 7 (**ANAPC7**) may also lead to triglyceride accumulation. ANAPC7, which is a component of the anaphase promoting complex/cyclosome (APC/C) (*63*), interacts with the CBP/p300 coactivator and stimulates its acetyl transferase activity (*64*). Among the CBP/p300 targets is farnesoid X receptor (FXR) (*65*). Acetylation of FXR leads to protein stabilization but reduces its activity as transcriptional regulator (*66*). Thus, reduced FXR acetylation resulting from ANAPC7 downregulation might activate FXR signaling. FXR signaling may induce lipid accumulation and reduced fatty acid oxidation (*67-69*). However, some reports show the opposite effect of FXR signaling on lipid accumulation (*70, 71*), suggesting perhaps context-specific effects.

3. Metabolism-related gene-level analysis of monocyte-derived macrophages treated with ACHN culture medium.

The top five up- and down-regulated genes (**Table S5a**) and functionally related, differentially expressed genes (**Table S5b**) were determined as described above for *M. tuberculosis* infection.

The top upregulated genes are enriched for glycolytic genes. Increased expression of hexokinase 3 (**HK3**) and other glycolytic genes (PFKFB4) might result in increased production of fructose 1,6-bisphosphate, which breaks down into dihydroxyacetone phosphate (DHAP) and glyceraldehyde 3-phosphate (G3P) (*37, 72*). Upregulation of triosephosphate isomerase (**TPI1**) also contributes to the conversion of DHAP to G3P, favoring triglyceride synthesis (*73*). G3P formation can also lead to synthesis of phosphoenolpyruvate (PEP), due to upregulation of other glycolytic genes (**PGK1**, **ENO2**) (*33*). Accumulation of PEP may result in enhanced production of pyruvate. Reduced utilization of pyruvate in the TCA cycle, which may be downregulated (see below), might lead to enhanced lipogenesis (*34*).

Macrophages treated with ACHN medium also exhibit transcriptional markers of reduced production/activity of the energy sensor AMP-activated protein kinase (AMPK). One is the upregulation of adenylate kinase 4 (**AK4**), which regulates cellular ATP levels and inhibits AMPK signaling (*74*). Another is the downregulation of phospholipase D family member 6 (**PLD6**), which activates AMPK by altering mitochondrial fusion and fission dynamics (*75*). The resulting decreased activity of AMPK, an energy sensor maintaining energy homeostasis (*76*), might result in increased YAP/TAZ signaling, which regulates metastasis and metabolic reprogramming in cancer cells (*77*), since AMPK inhibits YAP/TAZ via YAP phosphorylation (*78*). This scenario is suggested by the observed upregulation of genes associated with or regulated by YAP/TAZ, such as TEAD3, SLC2A5, and PLIN5, in ACHN-medium-treated macrophages. YAP/TAZ interacts with the TEAD transcription factors (*79*) to induce various target genes. One is the fructose transporter SLC2A5; its upregulation might result in increased fructose uptake, leading to lipogenesis via fructolysis (*80, 81*). YAP/TAZ also induces PLIN5, a member of a family of lipid-droplet-associated proteins (*82*), which protects triglycerides from enzymatic degradation by inhibiting adipose triglyceride lipase (*83, 84*). More in general, YAP/TAZ signaling and lipid metabolism are intricately intertwined in cancer cells, and YAP/TAZ is involved in the metabolism of fatty acids and sterols (*77*)**,** suggesting a role of this signaling pathway also in the cholesterol accumulation detected in the ACHN-medium-treated cells.

We identified additional gene expression markers of lipid accumulation. Impaired fatty acid oxidation, which may result in lipid accumulation, is suggested by the downregulation of the acyl-CoA synthase **ACSM4** and functionally related genes, such as acyl-CoA conversion to acyl-carnitine (carnitine palmitoyl transferase I, CPT1) and oxidation of fatty aldehydes to fatty acids (aldehyde hydrogenases, ALDH genes) (*1-3, 6*). The downregulation of **N6AMT1**, which encodes a methyltransferase mostly implicated in DNA and protein modification, is also consistent with lipid accumulation, since this gene product has been associated with lipid catabolism and low triglyceride levels (*85, 86*) by yet unknown mechanisms.

One of the top five downregulated genes is peroxisome proliferator-activated receptor gamma coactivator 1-alpha (**PPARGC1a**), a transcriptional coactivator that regulates cellular metabolism (*87*). Downregulation of PPARGC1a is consistent with the observed downregulation of two of its target genes, NAD-dependent isocitrate dehydrogenase 3 catalytic subunit alpha (IDH3A) (*88*) and CD36. Isocitrate dehydrogenases catalyze the oxidative decarboxylation of isocitrate to 2-oxoglutarate, which is a rate-limiting step of the TCA cycle. Thus, IDH3A downregulation might result in TCA cycle disruption. An additional indicator of dampened TCA

cycle is the above-mentioned upregulation of **AK4**, since this adenylate kinase is associated with decreased expression of key TCA cycle genes (*89*). The scavenger receptor CD36 is a critical fatty acid sensor and regulator of lipid metabolism (*90, 91*). CD36 mediates fatty acid uptake, increases cholesterol efflux, and favors proteasomal degradation of HMG-CoA reductase, the rate-limiting enzyme in sterol synthesis (*92, 93*). CD36 downregulation might result in cholesterol accumulation, reduced fatty acid oxidation and mitochondrial function, and increased fatty acid storage (*92*). Thus, CD36 downregulation is consistent with increased accumulation of both cholesterol and triglycerides in ACHN-medium-treated cells. The decreased activity of AMPK proposed above would further decrease CD36 function, since AMPK promotes CD36 expression and translocation (*50*).

An additional marker of dysregulated cholesterol homeostasis is the downregulation of adenylate cyclase (**ADCY1**). In response to G-protein signaling, adenylate cyclases are activated and generate cyclic AMP (cAMP) (*94*). cAMP participates in various signal transduction mechanisms regulating adipogenesis, lipolysis, and cholesterol efflux (*94, 95*). Reduced cAMP production may be associated with decreased cholesterol efflux and decreased lipolysis (*94-97*).

Supplementary References

1. A. Rinaldi *et al.*, Impaired fatty acid metabolism perpetuates lipotoxicity along the transition to chronic kidney injury. *JCI Insight* **7**, (2022).
2. K. R. Dunning, M. R. Anastasi, V. J. Zhang, D. L. Russell, R. L. Robker, Regulation of fatty acid oxidation in mouse cumulus-oocyte complexes during maturation and modulation by PPAR agonists. *PLoS One* **9**, e87327 (2014).
3. F. Le Borgne, A. Ben Mohamed, M. Logerot, E. Garnier, J. Demarquoy, Changes in carnitine octanoyltransferase activity induce alteration in fatty acid metabolism. *Biochem Biophys Res Commun* **409**, 699-704 (2011).
4. W. B. Rizzo, Fatty aldehyde and fatty alcohol metabolism: review and importance for epidermal structure and function. *Biochim Biophys Acta* **1841**, 377-389 (2014).
5. W. B. Rizzo, Sjogren-Larsson syndrome: molecular genetics and biochemical pathogenesis of fatty aldehyde dehydrogenase deficiency. *Mol Genet Metab* **90**, 1-9 (2007).
6. S. Li, Z. Yang, H. Zhang, M. Peng, H. Ma, Potential role of ALDH3A2 on the lipid and glucose metabolism regulated by (-)-hydroxycitric acid in chicken embryos. *Anim Sci J* **90**, 961-976 (2019).
7. S. A. Summers, Ceramides: Nutrient Signals that Drive Hepatosteatosis. *J Lipid Atheroscler* **9**, 50-65 (2020).
8. K. Nakahara *et al.*, The Sjogren-Larsson syndrome gene encodes a hexadecenal dehydrogenase of the sphingosine 1-phosphate degradation pathway. *Mol Cell* **46**, 461-471 (2012).
9. M. Bektas *et al.*, Sphingosine 1-phosphate lyase deficiency disrupts lipid homeostasis in liver. *J Biol Chem* **285**, 10880-10889 (2010).
10. A. Maharaj *et al.*, Isolated glucocorticoid deficiency: Genetic causes and animal models. *J Steroid Biochem Mol Biol* **189**, 73-80 (2019).
11. R. Wang *et al.*, Identification of palmitoyl protein thioesterase 1 in human THP1 monocytes and macrophages and characterization of unique biochemical activities for this enzyme. *Biochemistry* **52**, 7559-7574 (2013).
12. A. Khaibullina *et al.*, In a model of Batten disease, palmitoyl protein thioesterase-1 deficiency is associated with brown adipose tissue and thermoregulation abnormalities. *PLoS One* **7**, e48733 (2012).
13. Y. Jin *et al.*, Glutathione S-transferase Mu 2 inhibits hepatic steatosis via ASK1 suppression. *Commun Biol* **5**, 326 (2022).

14. R. Zhuo *et al.*, Targeting Glutathione S-transferase M4 in Ewing sarcoma. *Front Pediatr* **2**, 83 (2014).
15. X. F. Leong, Lipid Oxidation Products on Inflammation-Mediated Hypertension and Atherosclerosis: A Mini Review. *Front Nutr* **8**, 717740 (2021).
16. D. Cui *et al.*, FBXW7 Confers Radiation Survival by Targeting p53 for Degradation. *Cell Rep* **30**, 497-509 e494 (2020).
17. J. Tang *et al.*, Critical role for Daxx in regulating Mdm2. *Nat Cell Biol* **8**, 855-862 (2006).
18. R. U. Janicke, D. Sohn, K. Schulze-Osthoff, The dark side of a tumor suppressor: anti-apoptotic p53. *Cell Death Differ* **15**, 959-976 (2008).
19. C. Huang *et al.*, Identification of XBP1-u as a novel regulator of the MDM2/p53 axis using an shRNA library. *Sci Adv* **3**, e1701383 (2017).
20. H. Chen *et al.*, DEP domain-containing mTOR-interacting protein suppresses lipogenesis and ameliorates hepatic steatosis and acute-on-chronic liver injury in alcoholic liver disease. *Hepatology* **68**, 496-514 (2018).
21. V. Catena, M. Fanciulli, Deptor: not only a mTOR inhibitor. *J Exp Clin Cancer Res* **36**, 12 (2017).
22. G. A. Soliman, The integral role of mTOR in lipid metabolism. *Cell Cycle* **10**, 861-862 (2011).
23. M. Laplante, D. M. Sabatini, An emerging role of mTOR in lipid biosynthesis. *Curr Biol* **19**, R1046-1052 (2009).
24. S. Ruf *et al.*, PLK1 (polo like kinase 1) inhibits MTOR complex 1 and promotes autophagy. *Autophagy* **13**, 486-505 (2017).
25. S. Zhu *et al.*, Regulation of Glucose, Fatty Acid and Amino Acid Metabolism by Ubiquitination and SUMOylation for Cancer Progression. *Front Cell Dev Biol* **10**, 849625 (2022).
26. S. Lambhate, D. Bhattacharjee, N. Jain, APC/C CDH1 ubiquitinates IDH2 contributing to ROS increase in mitosis. *Cell Signal* **86**, 110087 (2021).
27. X. Qiao, L. Zhang, A. M. Gamper, T. Fujita, Y. Wan, APC/C-Cdh1: from cell cycle to cellular differentiation and genomic integrity. *Cell Cycle* **9**, 3904-3912 (2010).
28. M. Li, C. L. Brooks, N. Kon, W. Gu, A dynamic role of HAUSP in the p53-Mdm2 pathway. *Mol Cell* **13**, 879-886 (2004).
29. W. Ni *et al.*, USP7 mediates pathological hepatic de novo lipogenesis through promoting stabilization and transcription of ZNF638. *Cell Death Dis* **11**, 843 (2020).

30. R. Miao *et al.*, Akt: A Potential Drug Target for Metabolic Syndrome. *Front Physiol* **13**, 822333 (2022).
31. Z. Zhang *et al.*, Plk1 inhibition enhances the efficacy of androgen signaling blockade in castration-resistant prostate cancer. *Cancer Res* **74**, 6635-6647 (2014).
32. L. Jiang *et al.*, Ubiquitin-specific peptidase 7 (USP7)-mediated deubiquitination of the histone deacetylase SIRT7 regulates gluconeogenesis. *J Biol Chem* **292**, 13296-13311 (2017).
33. M. Yang *et al.*, Hypoxia-induced MIF induces dysregulation of lipid metabolism in Hep2 laryngocarcinoma through the IL-6/JAK-STAT pathway. *Lipids Health Dis* **21**, 82 (2022).
34. P. C. Ho *et al.*, Phosphoenolpyruvate Is a Metabolic Checkpoint of Anti-tumor T Cell Responses. *Cell* **162**, 1217-1228 (2015).
35. J. Bi *et al.*, Seipin promotes adipose tissue fat storage through the ER Ca(2)(+)-ATPase SERCA. *Cell Metab* **19**, 861-871 (2014).
36. S. Fu *et al.*, Aberrant lipid metabolism disrupts calcium homeostasis causing liver endoplasmic reticulum stress in obesity. *Nature* **473**, 528-531 (2011).
37. L. H. Fairley *et al.*, Mitochondrial control of microglial phagocytosis by the translocator protein and hexokinase 2 in Alzheimer's disease. *Proc Natl Acad Sci U S A* **120**, e2209177120 (2023).
38. L. Leng *et al.*, Microglial hexokinase 2 deficiency increases ATP generation through lipid metabolism leading to β-amyloid clearance. *Nat Metab* **4**, 1287-1305 (2022).
39. X. Li *et al.*, Mitochondria-Translocated PGK1 Functions as a Protein Kinase to Coordinate Glycolysis and the TCA Cycle in Tumorigenesis. *Mol Cell* **61**, 705-719 (2016).
40. L. Xu *et al.*, SIRT3 elicited an anti-Warburg effect through HIF1alpha/PDK1/PDHA1 to inhibit cholangiocarcinoma tumorigenesis. *Cancer Med* **8**, 2380-2391 (2019).
41. S. Chen, L. Zhou, J. Sun, Y. Qu, M. Chen, The Role of cAMP-PKA Pathway in Lactate-Induced Intramuscular Triglyceride Accumulation and Mitochondria Content Increase in Mice. *Front Physiol* **12**, 709135 (2021).
42. C. Liu *et al.*, Lactate inhibits lipolysis in fat cells through activation of an orphan G-protein-coupled receptor, GPR81. *J Biol Chem* **284**, 2811-2822 (2009).
43. V. Vedrenne *et al.*, Mutation in PNPT1, which encodes a polyribonucleotide nucleotidyltransferase, impairs RNA import into mitochondria and causes respiratory-chain deficiency. *Am J Hum Genet* **91**, 912-918 (2012).

44. G. Wang *et al.*, PNPASE regulates RNA import into mitochondria. *Cell* **142**, 456-467 (2010).
45. M. Kohda *et al.*, A Comprehensive Genomic Analysis Reveals the Genetic Landscape of Mitochondrial Respiratory Chain Complex Deficiencies. *PLoS Genet* **12**, e1005679 (2016).
46. F. Dursun *et al.*, Primary adrenal insufficiency in a patient with biallelic QRSL1 mutations. *Eur J Endocrinol* **187**, K27-K32 (2022).
47. K. Puri *et al.*, Diabetes Mellitus Severity and a Switch From Using Lipoprotein Lipase to Adipose-Derived Fatty Acid Results in a Cardiac Metabolic Signature That Embraces Cell Death. *J Am Heart Assoc* **8**, e014022 (2019).
48. D. Hathazi *et al.*, Metabolic shift underlies recovery in reversible infantile respiratory chain deficiency. *EMBO J* **39**, e105364 (2020).
49. M. Foretz, P. C. Even, B. Viollet, AMPK Activation Reduces Hepatic Lipid Content by Increasing Fat Oxidation In Vivo. *Int J Mol Sci* **19**, (2018).
50. W. Wu *et al.*, AMPK facilitates intestinal long-chain fatty acid uptake by manipulating CD36 expression and translocation. *FASEB J* **34**, 4852-4869 (2020).
51. H. Wu *et al.*, Lipid droplet-dependent fatty acid metabolism controls the immune suppressive phenotype of tumor-associated macrophages. *EMBO Mol Med* **11**, e10698 (2019).
52. D. L. Brasaemle, Thematic review series: adipocyte biology. The perilipin family of structural lipid droplet proteins: stabilization of lipid droplets and control of lipolysis. *J Lipid Res* **48**, 2547-2559 (2007).
53. L. C. Lin, A. C. Gao, C. H. Lai, J. T. Hsieh, H. Lin, Induction of neuroendocrine differentiation in castration resistant prostate cancer cells by adipocyte differentiation-related protein (ADRP) delivered by exosomes. *Cancer Lett* **391**, 74-82 (2017).
54. J. Sun *et al.*, The 11S Proteasome Subunit PSME3 Is a Positive Feedforward Regulator of NF-kappaB and Important for Host Defense against Bacterial Pathogens. *Cell Rep* **14**, 737-749 (2016).
55. V. G. Yerra, K. Drosatos, Specificity Proteins (SP) and Krüppel-like Factors (KLF) in Liver Physiology and Pathology. *Int J Mol Sci* **24**, (2023).
56. J. Ling *et al.*, Defective lipid metabolism associated with mutation in klf-2 and klf-3: important roles of essential dietary salts in fat storage. *Nutr Metab (Lond)* **14**, 22 (2017).
57. M. Matz-Soja *et al.*, Hedgehog signaling is a potent regulator of liver lipid metabolism and reveals a GLI-code associated with steatosis. *Elife* **5**, (2016).

58. G. D. Dalton *et al.*, Hepatocyte activity of the cholesterol sensor smoothened regulates cholesterol and bile acid homeostasis in mice. *iScience* **24**, 103089 (2021).
59. Z. Zhou *et al.*, The deubiquitinase UCHL5/UCH37 positively regulates Hedgehog signaling by deubiquitinating Smoothened. *J Mol Cell Biol* **10**, 243-257 (2018).
60. R. Tu *et al.*, The emerging role of deubiquitylating enzymes as therapeutic targets in cancer metabolism. *Cancer Cell Int* **22**, 130 (2022).
61. K. Petrov, T. de Almeida Magalhaes, A. Salic, Mechanism and ultrasensitivity in Hedgehog signaling revealed by Patched1 disease mutations. *Proc Natl Acad Sci U S A* **118**, (2021).
62. U. Styrkarsdottir *et al.*, Sequence variants in the PTCH1 gene associate with spine bone mineral density and osteoporotic fractures. *Nat Commun* **7**, 10129 (2016).
63. J. M. Peters, The anaphase-promoting complex: proteolysis in mitosis and beyond. *Mol Cell* **9**, 931-943 (2002).
64. J. Liu, S. Y. Fuchs, Cross-talk between APC/C and CBP/p300. *Cancer Biol Ther* **5**, 760-762 (2006).
65. S. Fang *et al.*, The p300 acetylase is critical for ligand-activated farnesoid X receptor (FXR) induction of SHP. *J Biol Chem* **283**, 35086-35095 (2008).
66. J. K. Kemper *et al.*, FXR acetylation is normally dynamically regulated by p300 and SIRT1 but constitutively elevated in metabolic disease states. *Cell Metab* **10**, 392-404 (2009).
67. K. H. Kim *et al.*, Hepatic FXR/SHP axis modulates systemic glucose and fatty acid homeostasis in aged mice. *Hepatology* **66**, 498-509 (2017).
68. K. Boulias *et al.*, Regulation of hepatic metabolic pathways by the orphan nuclear receptor SHP. *EMBO J* **24**, 2624-2633 (2005).
69. M. Abdelkarim *et al.*, The farnesoid X receptor regulates adipocyte differentiation and function by promoting peroxisome proliferator-activated receptor-gamma and interfering with the Wnt/beta-catenin pathways. *J Biol Chem* **285**, 36759-36767 (2010).
70. Y. Jiao, Y. Lu, X. Y. Li, Farnesoid X receptor: a master regulator of hepatic triglyceride and glucose homeostasis. *Acta Pharmacol Sin* **36**, 44-50 (2015).
71. G. Y. Wu *et al.*, MicroRNA-122 Inhibits Lipid Droplet Formation and Hepatic Triglyceride Accumulation via Yin Yang 1. *Cell Physiol Biochem* **44**, 1651-1664 (2017).
72. W. Xu *et al.*, Hexokinase 3 dysfunction promotes tumorigenesis and immune escape by upregulating monocyte/macrophage infiltration into the clear cell renal cell carcinoma microenvironment. *Int J Biol Sci* **17**, 2205-2222 (2021).

73. G. A. Rao, M. F. Sorrels, R. Reiser, Biosynthesis of triglycerides from triose phosphates by microsomes of intestinal mucosa. *Lipids* **5**, 762-764 (1970).
74. N. J. Lanning *et al.*, A mitochondrial RNAi screen defines cellular bioenergetic determinants and identifies an adenylate kinase as a key regulator of ATP levels. *Cell Rep* **7**, 907-917 (2014).
75. B. von Eyss *et al.*, A MYC-Driven Change in Mitochondrial Dynamics Limits YAP/TAZ Function in Mammary Epithelial Cells and Breast Cancer. *Cancer Cell* **28**, 743-757 (2015).
76. G. R. Steinberg, D. G. Hardie, New insights into activation and function of the AMPK. *Nat Rev Mol Cell Biol* **24**, 255-272 (2023).
77. H. Yamaguchi, G. M. Taouk, A Potential Role of YAP/TAZ in the Interplay Between Metastasis and Metabolic Alterations. *Front Oncol* **10**, 928 (2020).
78. J. S. Mo *et al.*, Cellular energy stress induces AMPK-mediated regulation of YAP and the Hippo pathway. *Nat Cell Biol* **17**, 500-510 (2015).
79. I. M. Moya, G. Halder, Hippo-YAP/TAZ signalling in organ regeneration and regenerative medicine. *Nat Rev Mol Cell Biol* **20**, 211-226 (2019).
80. H. D. Huh, D. H. Kim, H. S. Jeong, H. W. Park, Regulation of TEAD Transcription Factors in Cancer Biology. *Cells* **8**, (2019).
81. K. W. Ter Horst, M. J. Serlie, Fructose Consumption, Lipogenesis, and Non-Alcoholic Fatty Liver Disease. *Nutrients* **9**, (2017).
82. H. Itabe, T. Yamaguchi, S. Nimura, N. Sasabe, Perilipins: a diversity of intracellular lipid droplet proteins. *Lipids Health Dis* **16**, 83 (2017).
83. H. Wang *et al.*, Unique regulation of adipose triglyceride lipase (ATGL) by perilipin 5, a lipid droplet-associated protein. *J Biol Chem* **286**, 15707-15715 (2011).
84. L. L. Listenberger, A. G. Ostermeyer-Fay, E. B. Goldberg, W. J. Brown, D. A. Brown, Adipocyte differentiation-related protein reduces the lipid droplet association of adipose triglyceride lipase and slows triacylglycerol turnover. *J Lipid Res* **48**, 2751-2761 (2007).
85. R. C. Slieker *et al.*, Identification of biomarkers for glycaemic deterioration in type 2 diabetes. *Nat Commun* **14**, 2533 (2023).
86. Z. Si *et al.*, Identification of CYP46A1 as a new regulator of lipid metabolism through CRISPR-based whole-genome screening. *Faseb j* **34**, 13776-13791 (2020).
87. C. F. Cheng, H. C. Ku, H. Lin, PGC-1α as a Pivotal Factor in Lipid and Metabolic Regulation. *Int J Mol Sci* **19**, (2018).

88. Q. Zhang *et al.*, MiR-30b-5p regulates the lipid metabolism by targeting PPARGC1A in Huh-7 cell line. *Lipids Health Dis* **19**, 76 (2020).
89. K. Fujisawa *et al.*, Modulation of anti-cancer drug sensitivity through the regulation of mitochondrial activity by adenylate kinase 4. *Journal of Experimental & Clinical Cancer Research* **35**, 48 (2016).
90. Y. Li *et al.*, CD36 favours fat sensing and transport to govern lipid metabolism. *Prog Lipid Res* **88**, 101193 (2022).
91. R. L. Silverstein, M. Febbraio, CD36, a scavenger receptor involved in immunity, metabolism, angiogenesis, and behavior. *Sci Signal* **2**, re3 (2009).
92. L. Marechal *et al.*, The CD36-PPARgamma Pathway in Metabolic Disorders. *Int J Mol Sci* **19**, (2018).
93. A. Rodrigue-Way *et al.*, Scavenger receptor CD36 mediates inhibition of cholesterol synthesis via activation of the PPARγ/PGC-1α pathway and Insig1/2 expression in hepatocytes. *Faseb j* **28**, 1910-1923 (2014).
94. M. Rogne, K. Tasken, Compartmentalization of cAMP signaling in adipogenesis, lipogenesis, and lipolysis. *Horm Metab Res* **46**, 833-840 (2014).
95. W. Tang *et al.*, Adenylyl cyclase 1 as a major isoform to generate cAMP signaling for apoA-1-mediated cholesterol efflux pathway. *J Lipid Res* **59**, 635-645 (2018).
96. B. M. Stenson *et al.*, Liver X receptor (LXR) regulates human adipocyte lipolysis. *J Biol Chem* **286**, 370-379 (2011).
97. P. Arner, D. P. Andersson, J. Backdahl, I. Dahlman, M. Ryden, Weight Gain and Impaired Glucose Metabolism in Women Are Predicted by Inefficient Subcutaneous Fat Cell Lipolysis. *Cell Metab* **28**, 45-54 e43 (2018).